Supplementary Material

Dualistic correlated phases induced by interlayer sliding in few layer Ta_2NiS_5

Yu Yang[1], Yulu Liu[2], Ke Yang[3,4], Yan Zhou[1], Qingxuan Wang[1], Ning Zhao[1], Jun Zhou[1], Ming Yang[3,4], Xiaoxiang Xi[2], Lifa Zhang[1, *] and Yunshan Zhao[1, *]

[1]Phonon Engineering Research Center of Jiangsu Province, Ministry of Education Key Laboratory of NSLSCS, Center for Quantum Transport and Thermal Energy Science, Institute of Physics Frontiers and Interdisciplinary Sciences, School of Physics and Technology, Nanjing Normal University, Nanjing 210023, China.

[2]National Laboratory of Solid State Microstructures, School of Physics, Collaborative Innovation Center of Advanced Microstructures, Jiangsu Physical Science Research Center, Nanjing University, Nanjing 210093, China.

[3]Department of Applied Physics, The Hong Kong Polytechnic University, Kowloon, Hong Kong SAR, China.

[4]Research Centre for Nanoscience and Nanotechnology, The Hong Kong Polytechnic University, Kowloon, Hong Kong SAR, China

[*]Corresponding authors. E-mails: phyzys@njnu.edu.cn; phyzlf@njnu.edu.cn;

This PDF file includes:

Supplementary Figure 1 to Supplementary Figure 54
Supplementary Table 1 to Supplementary Table 3
Supplementary Note 1 to Supplementary Note 5

This PDF file includes:

Supplementary Figures

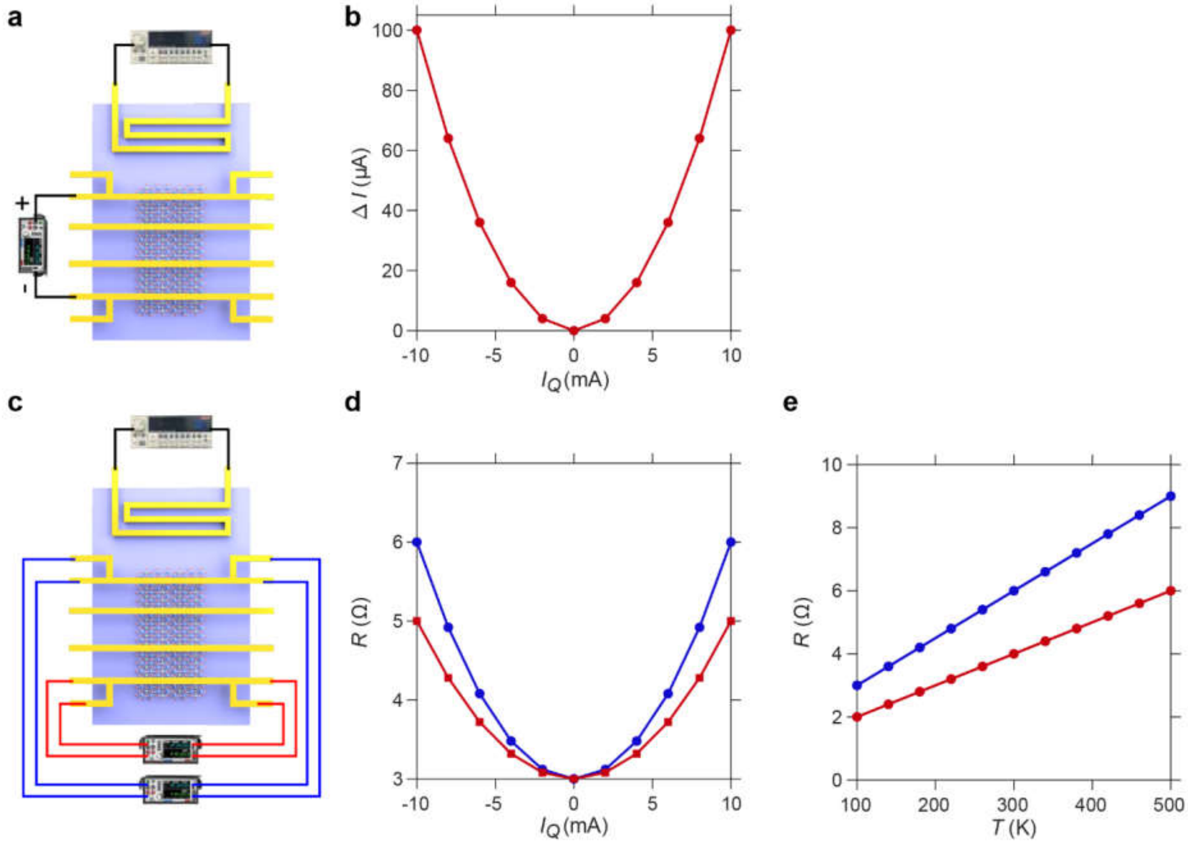

Supplementary Figure 1. Schematic diagram of measurement method for thermal induced current (TIC). a,b Schematic diagram of heater/meter setup (**a**) and the corresponding electronic current signal (**b**). **c-e** Schematic diagram of heater/meter setup (**c**) and the corresponding electronic resistance as a function of input heater current (**d**) and temperature (**e**) of temperature difference.

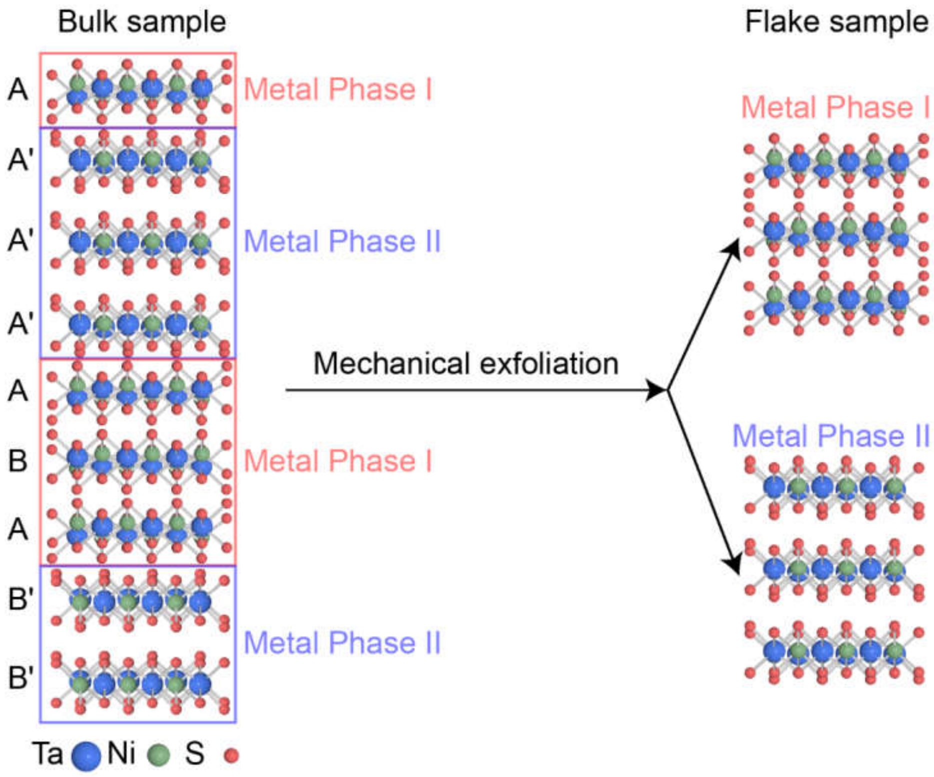

Supplementary Figure 2. Schematic diagram of phase distribution in a natural bulk Ta_2NiS_5 (TNS) crystal and a few-layer TNS flake after mechanical exfoliation.

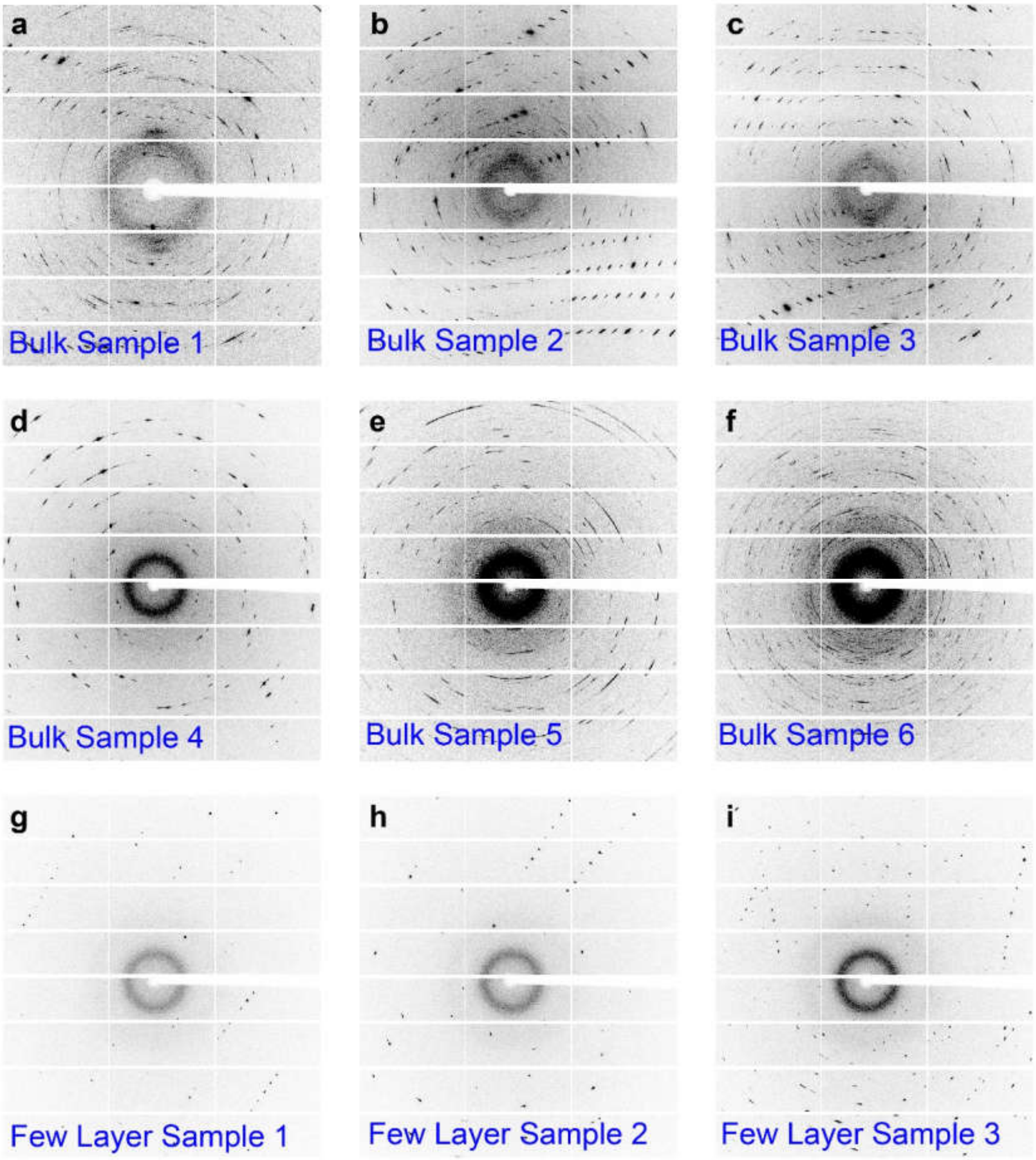

Supplementary Figure 3. High-energy synchrotron radiation X-ray diffraction measurement for bulk and few layer TNS flake. a-f High-energy synchrotron radiation X-ray diffraction measurement for various bulk TNS flakes. **g-i** High-energy synchrotron radiation X-ray diffraction measurement for various few layer TNS flakes.

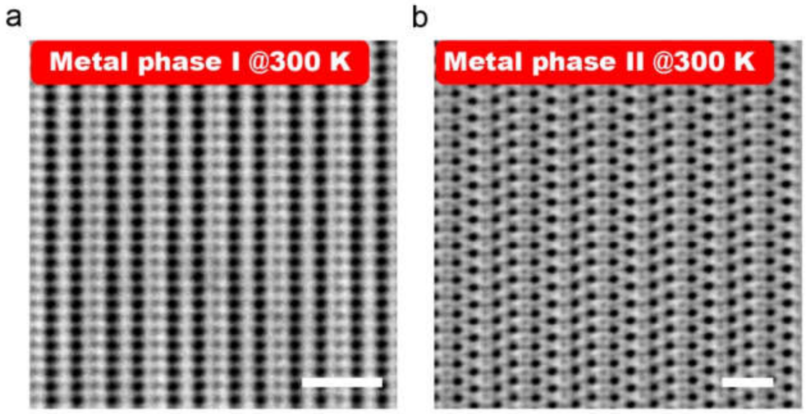

Supplementary Figure 4. Structural characterization of few layer TNS flakes. a,b Atomic-resolution bright-field scanning transmission electron microscope image of the Phase I (**a**) and Phase II (**b**) of few layer TNS flakes at 300 K, viewed along the [001] direction. The scale bar is 1 nm.

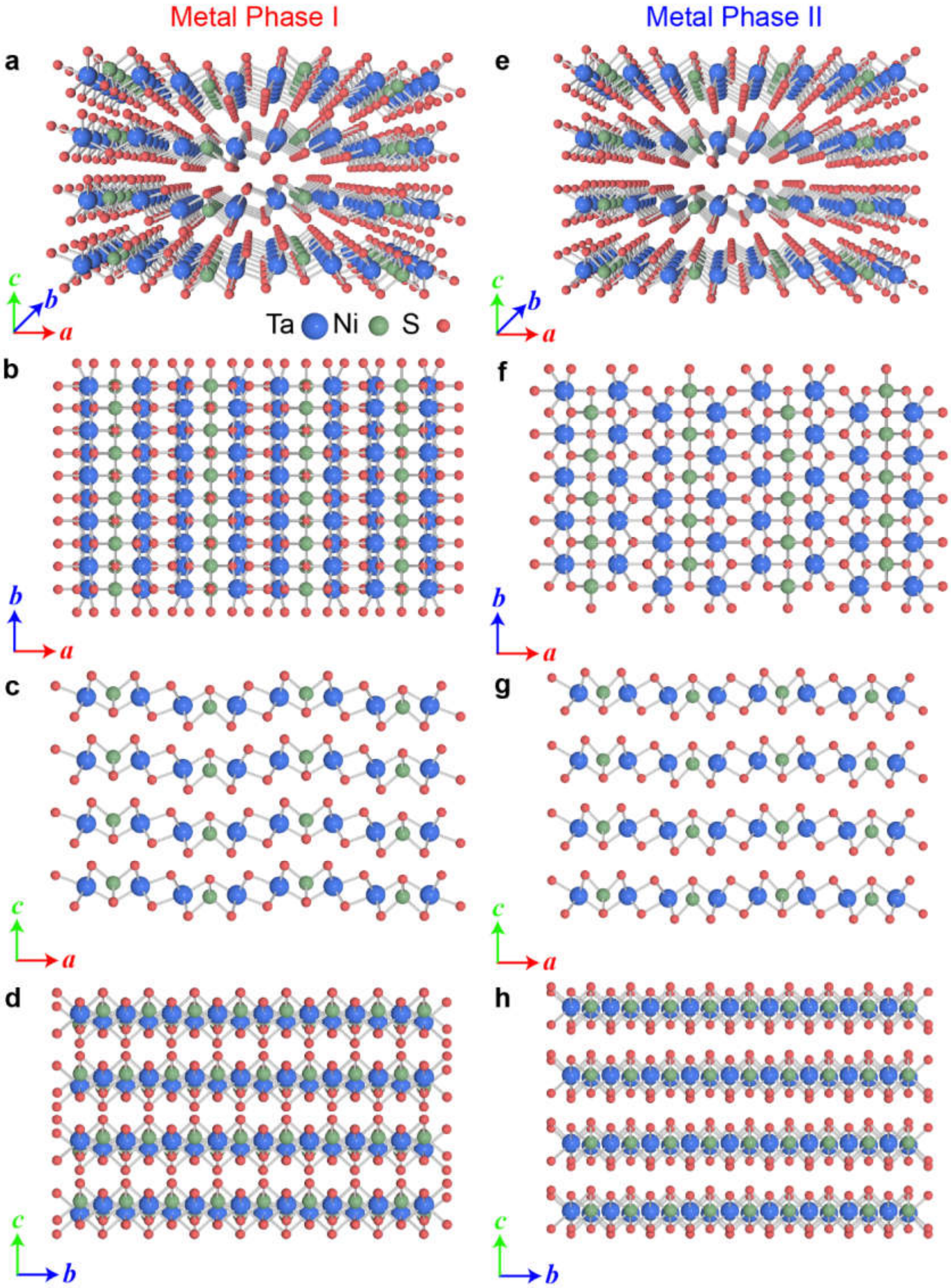

Supplementary Figure 5. Schematics of crystallographic structure for metal phase I and metal phase II in TNS crystal. a-d Schematics of crystallographic structure for metal phase I along different directions. **e-h** Schematics of crystallographic structure for metal phase II along different directions.

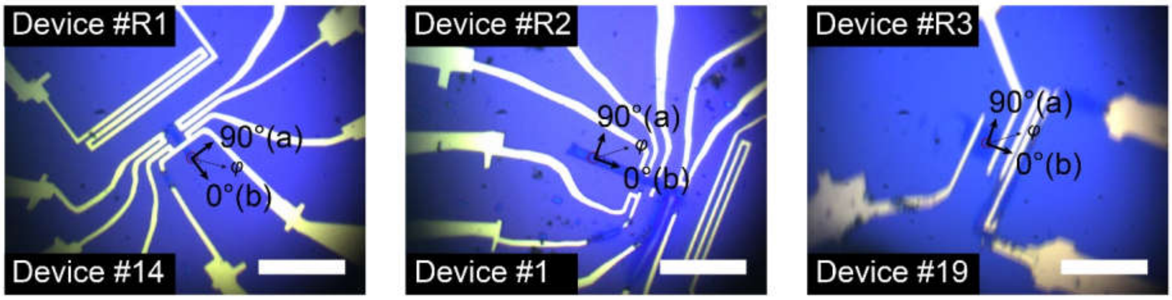

Supplementary Figure 6. Optical image of angle-resolved polarized Raman spectroscopy (ARPRS) devices. Optical image of the Device #R1 to #R3, which correspond to Devices 14, 1 and 19 respectively. The scale bar is 20 μm.

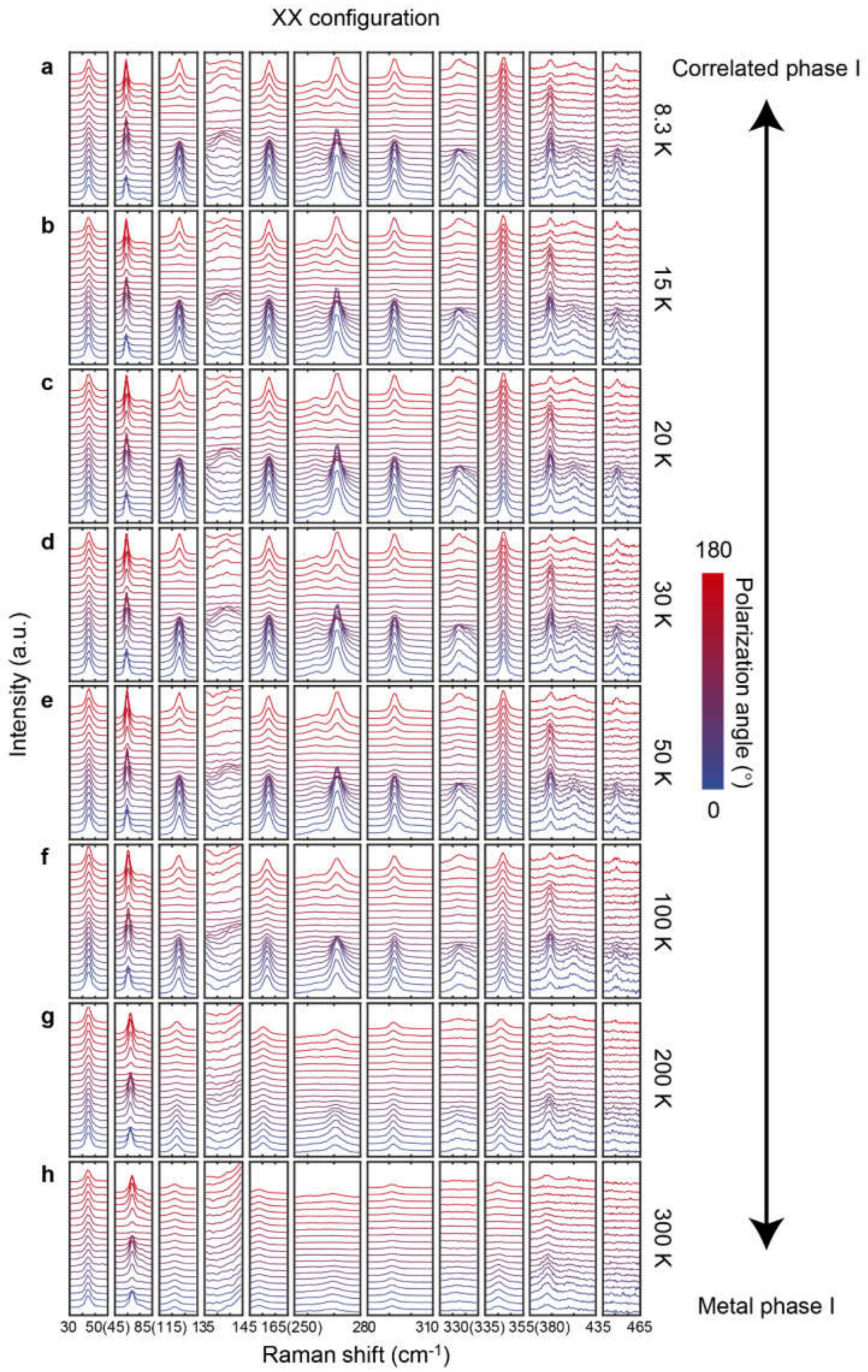

Supplementary Figure 7. Temperature dependent ARPRS of phase I in TNS under XX configuration. **a-h** Temperature dependent ARPRS of phase I in TNS under XX configuration at 8.3 K, 15 K, 20 K, 30 K, 50 K, 100 K, 200 K, 300 K. Color represents the polarization angle.

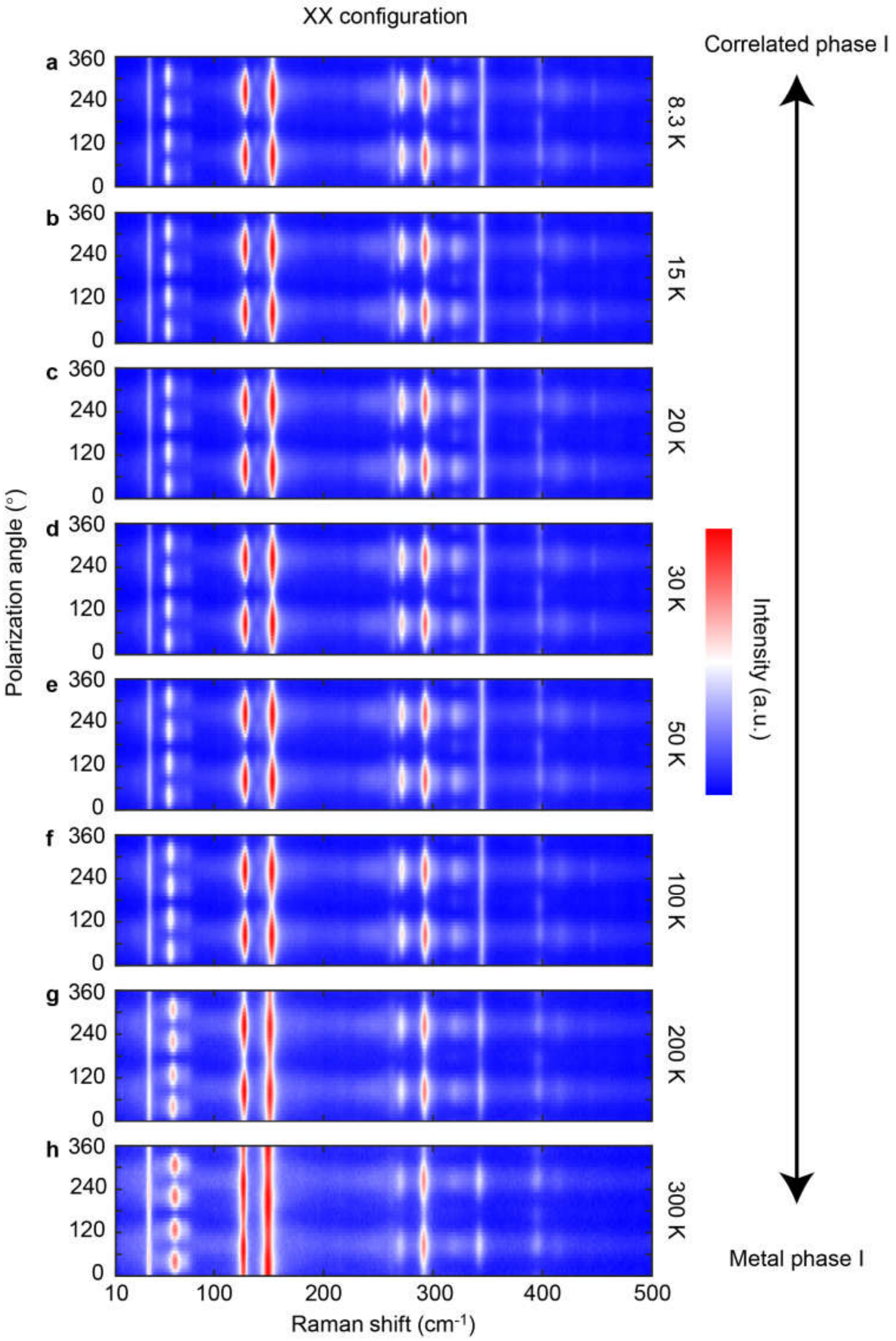

Supplementary Figure 8. Contour color map of temperature dependent ARPRS for phase I in TNS under XX configuration. a-h Contour color map of temperature dependent ARPRS for phase I in TNS under XX configuration at 8.3 K, 15 K, 20 K, 30 K, 50 K, 100 K, 200 K, 300 K. Color represents the Raman intensity.

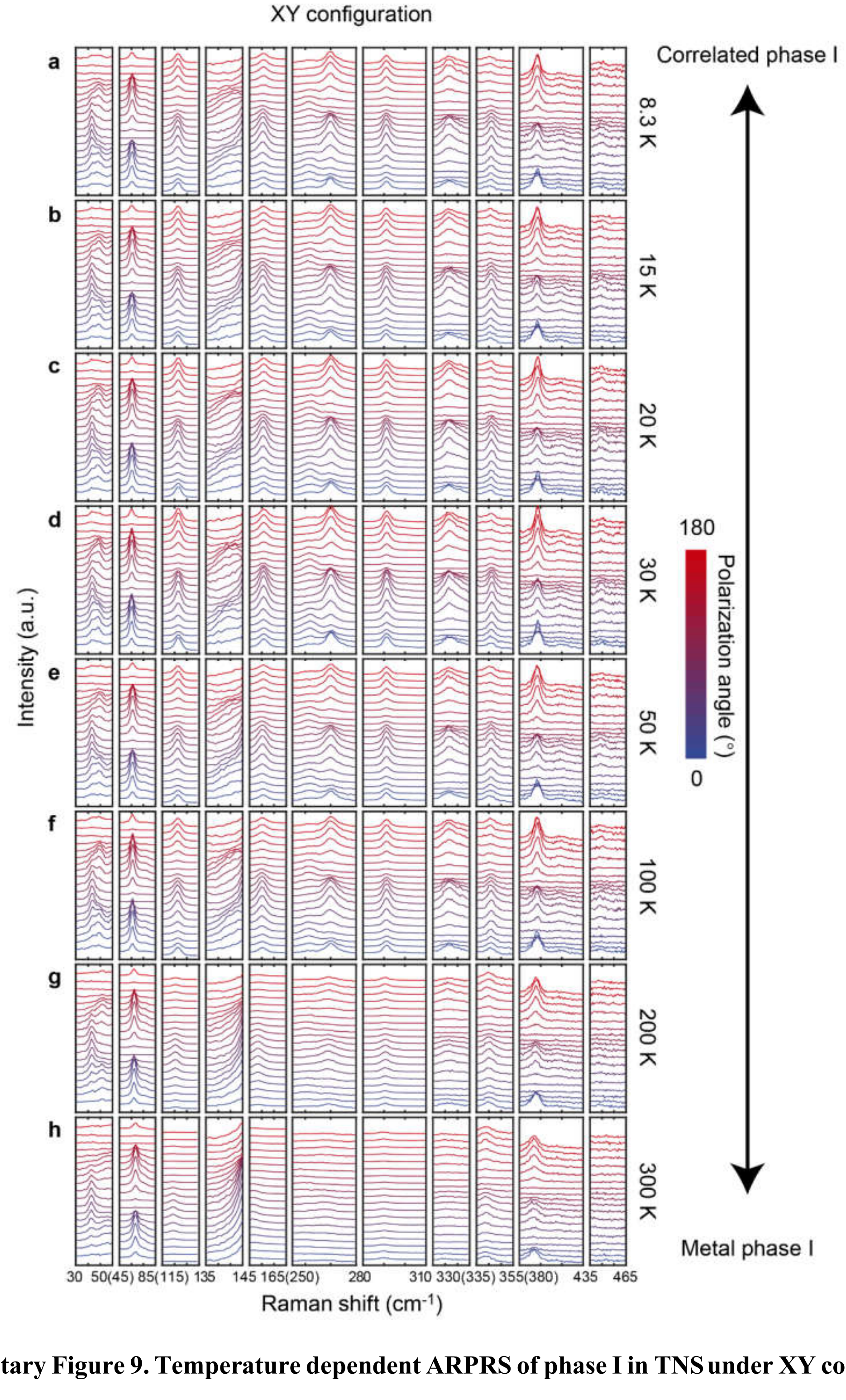

Supplementary Figure 9. Temperature dependent ARPRS of phase I in TNS under XY configuration. **a-h** Temperature dependent ARPRS for phase I in TNS under XY configuration at 8.3 K, 15 K, 20 K, 30 K, 50 K, 100 K, 200 K, 300 K. Color represents the polarization angle.

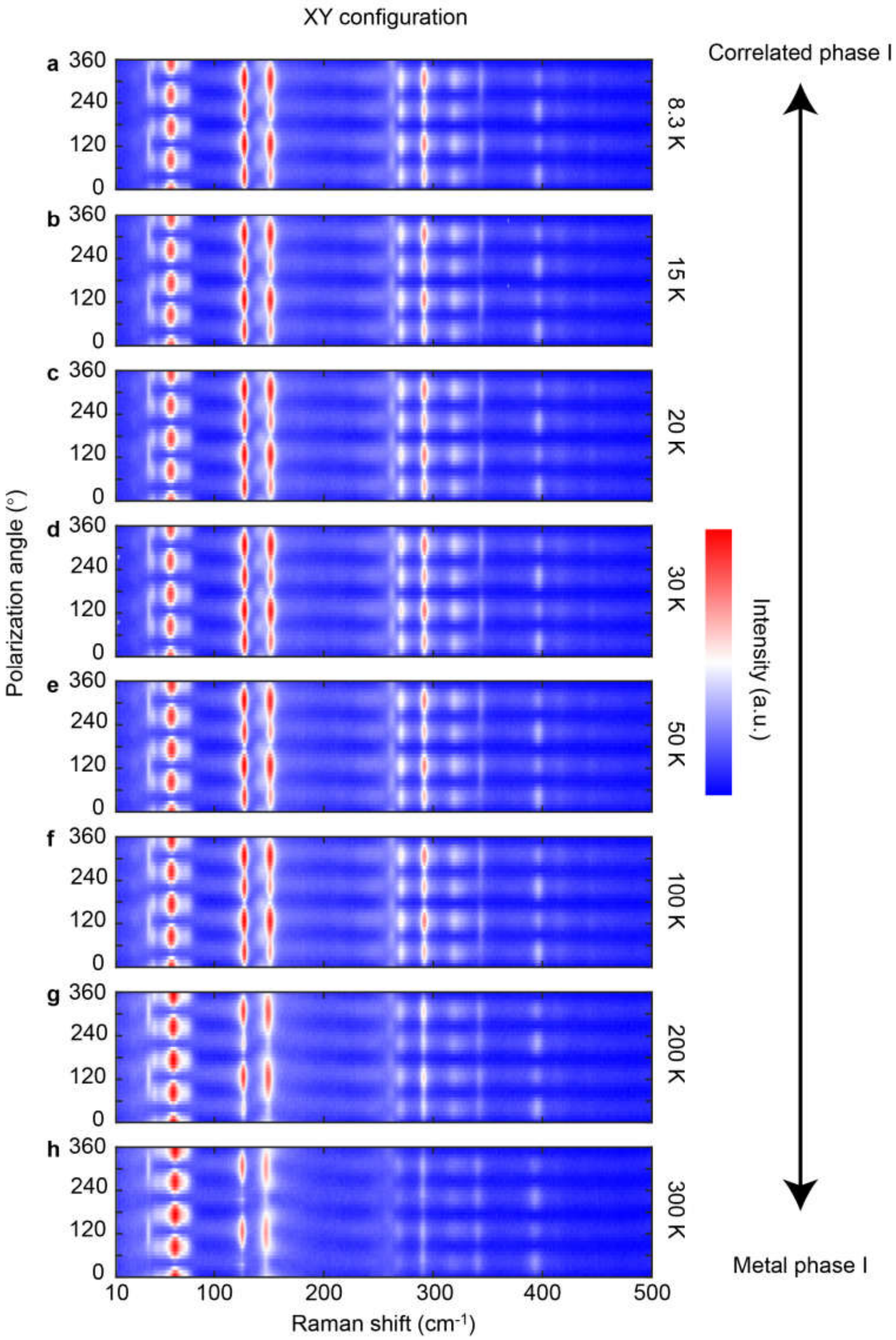

Supplementary Figure 10. Contour colour map of the temperature dependent ARPRS for phase I in TNS under XY configuration. a-h Contour color map of temperature dependent ARPRS for phase I in

TNS under XY configuration at 8.3 K, 15 K, 20 K, 30 K, 50 K, 100 K, 200 K, 300 K. Color represents the Raman intensity.

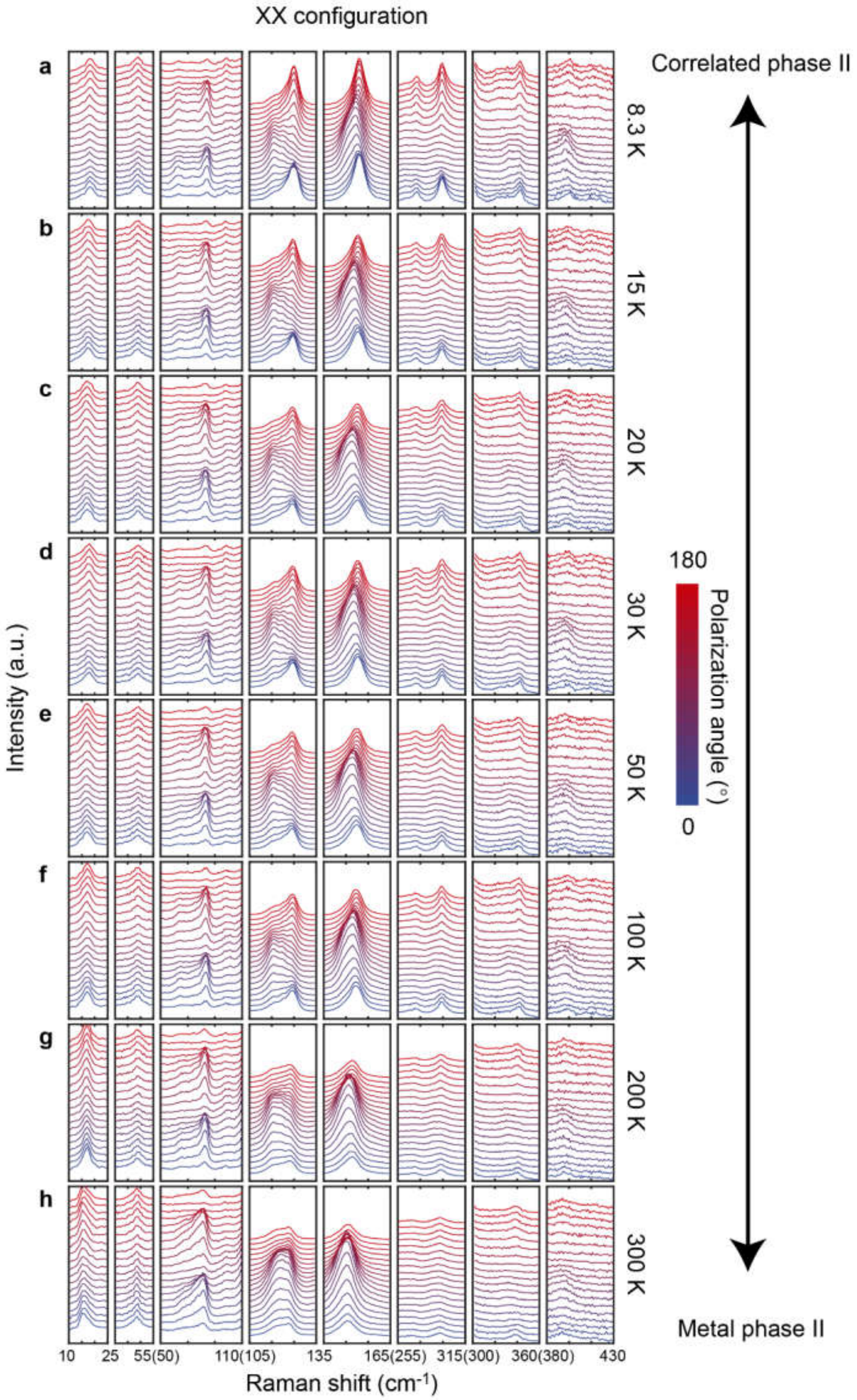

Supplementary Figure 11. Tmperature dependent ARPRS of phase II in TNS under XX configuration. a-h Temperature dependent ARPRS for phase II in TNS under XX configuration at 8.3 K, 15 K, 20 K, 30 K, 50 K, 100 K, 200 K, 300 K. Color represents the polarization angle.

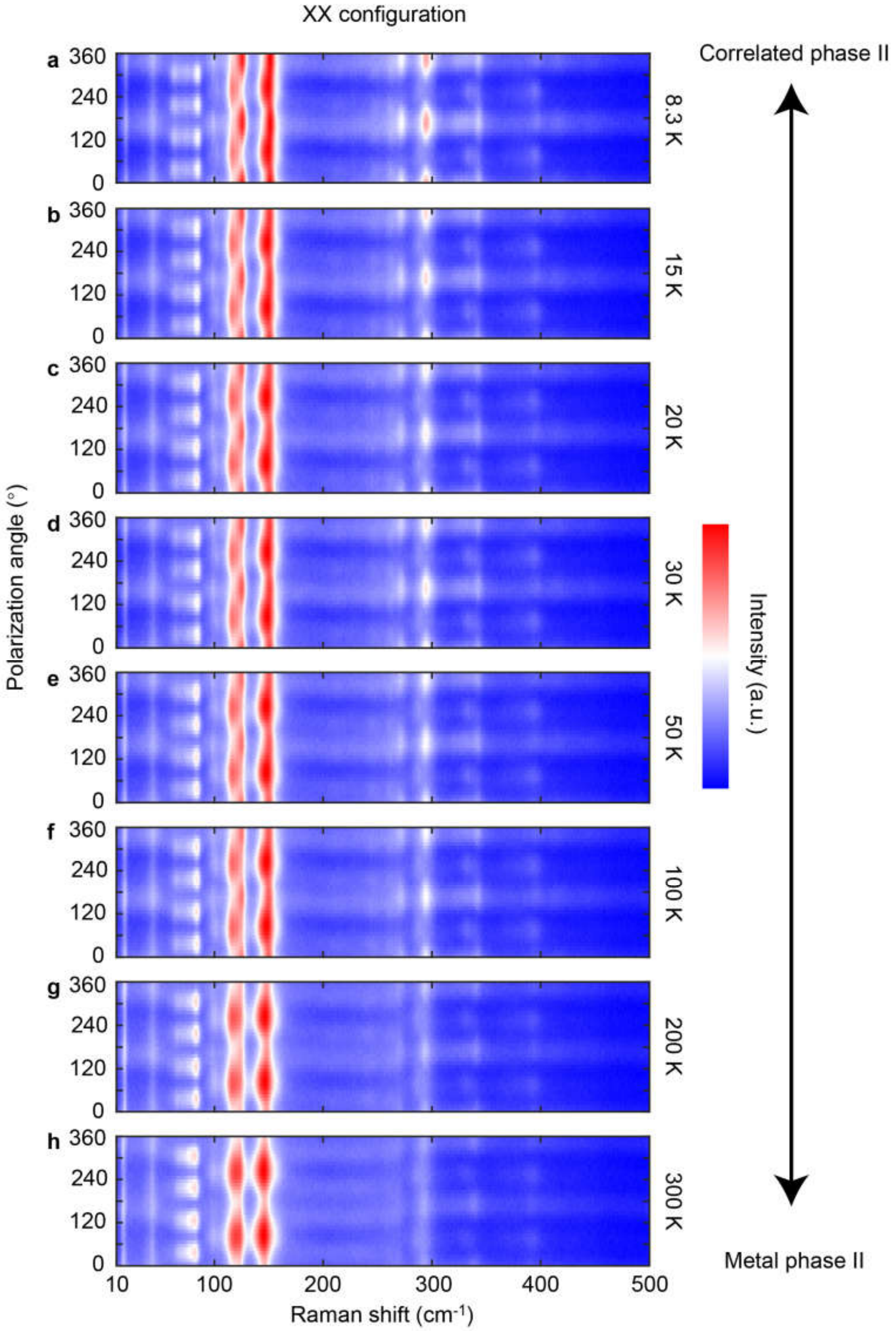

Supplementary Figure 12. Contour colour map of temperature dependent ARPRS for phase II in TNS under XX configuration. a-h Contour color map of temperature dependent ARPRS for phase II in

TNS under XX configuration at 8.3 K, 15 K, 20 K, 30 K, 50 K, 100 K, 200 K, 300 K. Color represents the Raman intensity.

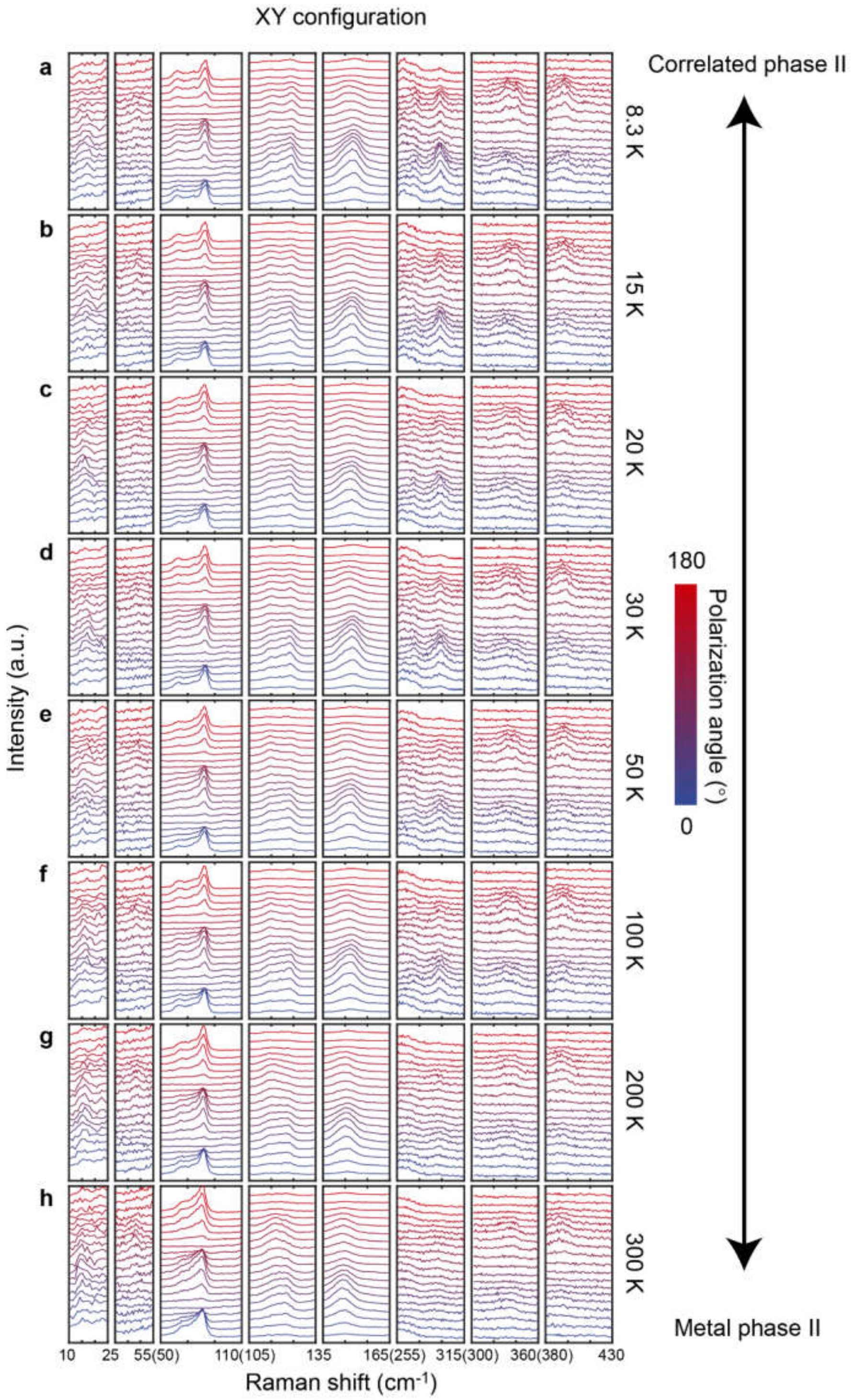

Supplementary Figure 13. Temperature dependent ARPRS of phase II in TNS under XY configuration. a-h Temperature dependent ARPRS for phase II in TNS under XY configuration at 8.3 K, 15 K, 20 K, 30 K, 50 K, 100 K, 200 K, 300 K. Color represents the polarization angle.

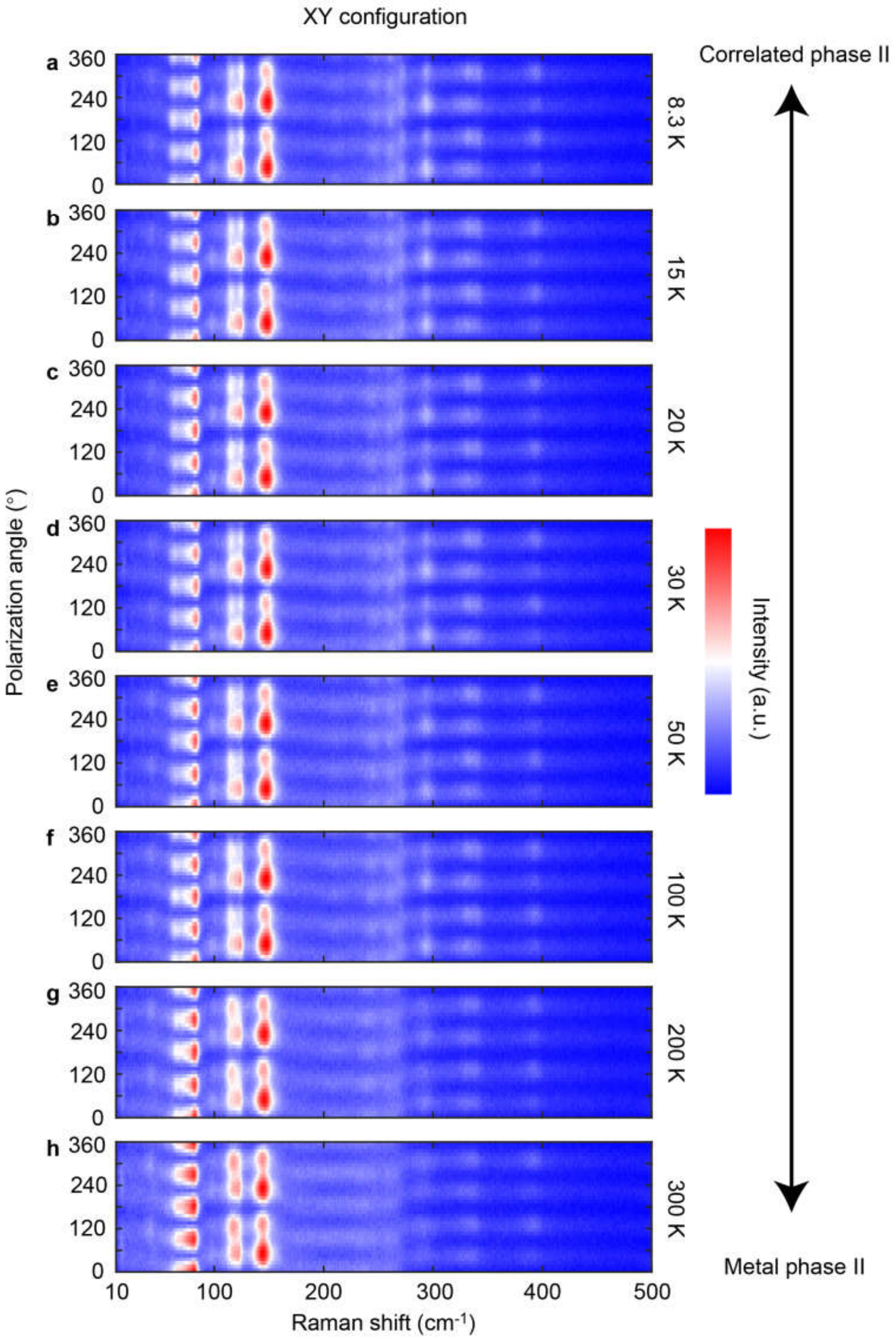

164

165 **Supplementary Figure 14. Contour colour map of temperature dependent ARPRS for phase II in**
166 **TNS under XY configuration. a-h** Contour color map of temperature dependent ARPRS for phase II in

TNS under XY configuration at 8.3 K, 15 K, 20 K, 30 K, 50 K, 100 K, 200 K, 300 K. Color represents the Raman intensity.

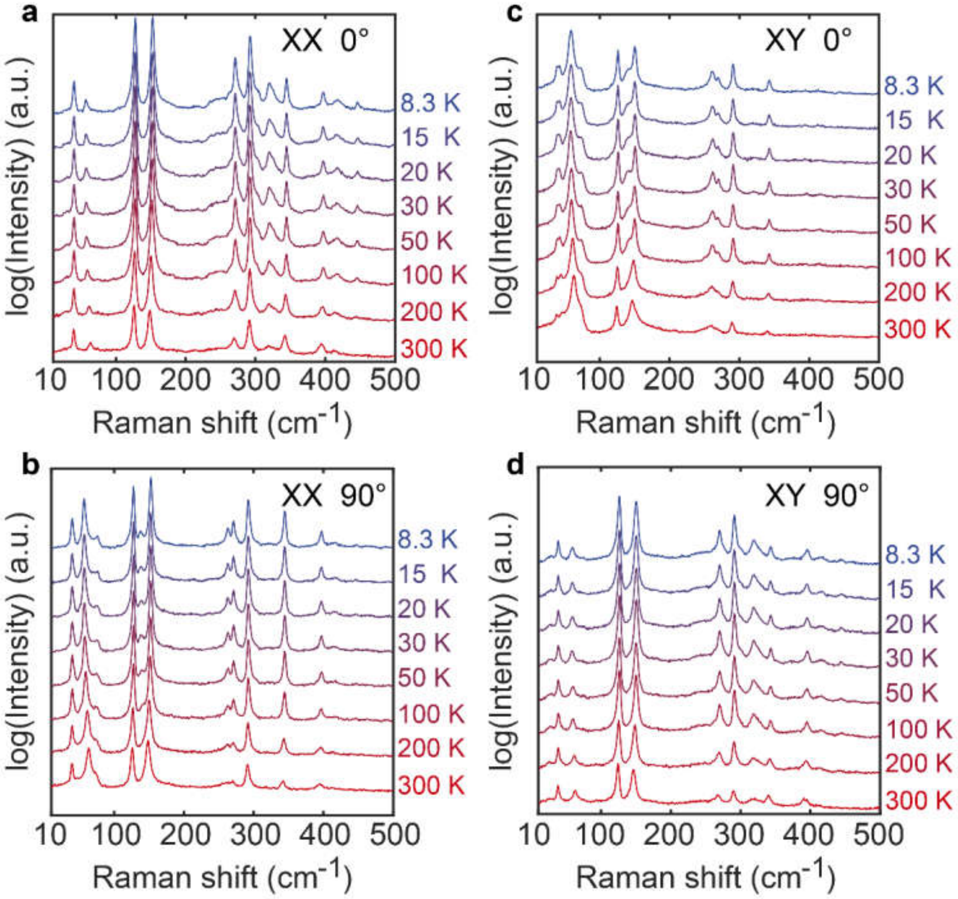

Supplementary Figure 15. Temperature dependent ARPRS of phase I in TNS under different configurations. a-d Temperature dependent ARPRS for phase I in TNS under XX and XY configurations at 8.3 K, 15 K, 20 K, 30 K, 50 K, 100 K, 200 K, 300 K. Color represents the temperature.

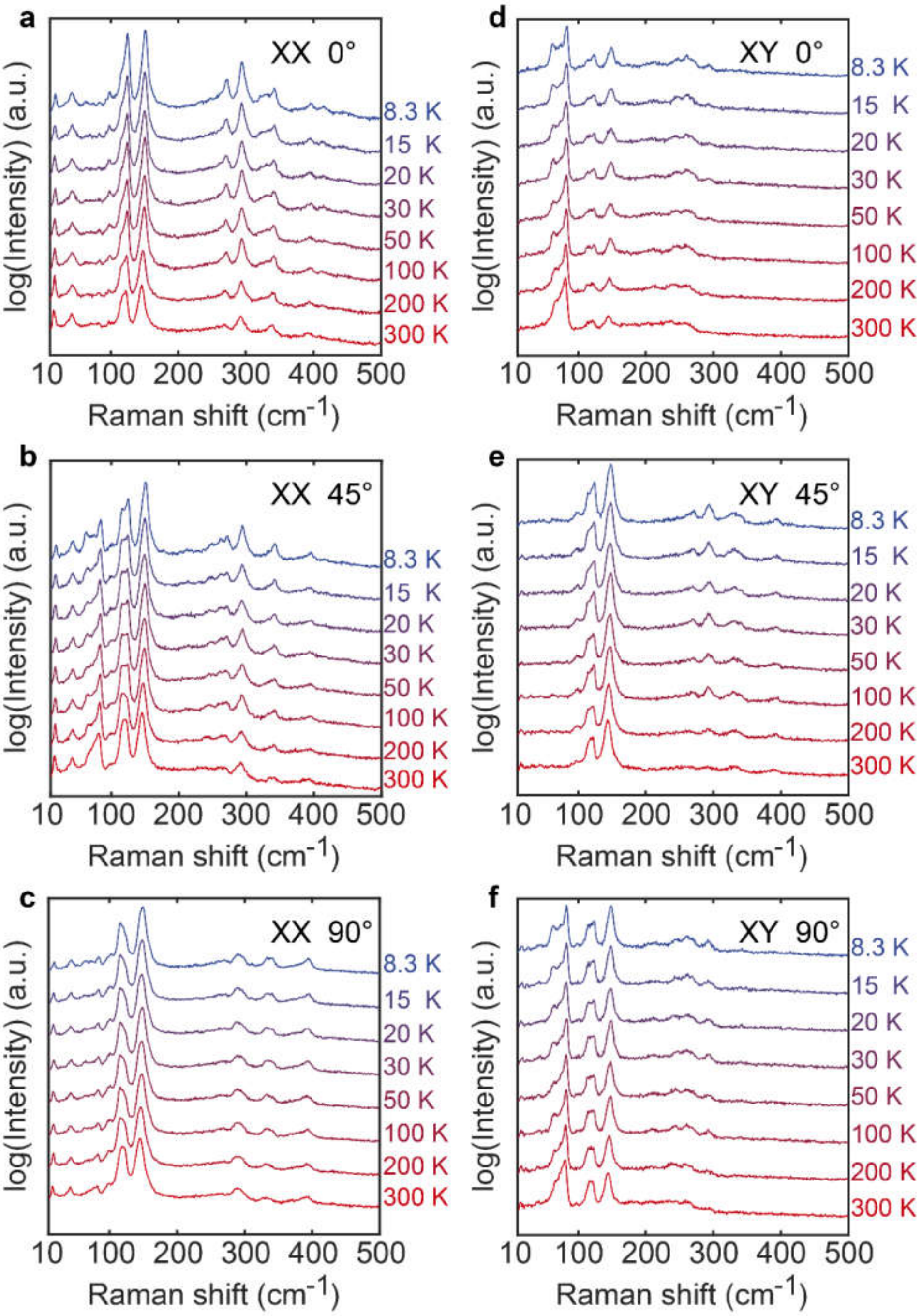

Supplementary Figure 16. Temperature dependent ARPRS of phase II in TNS under different configurations. a-f Temperature dependent ARPRS for phase II in TNS under XX and XY configurations at 8.3 K, 15 K, 20 K, 30 K, 50 K, 100 K, 200 K, 300 K. Color represents the temperature.

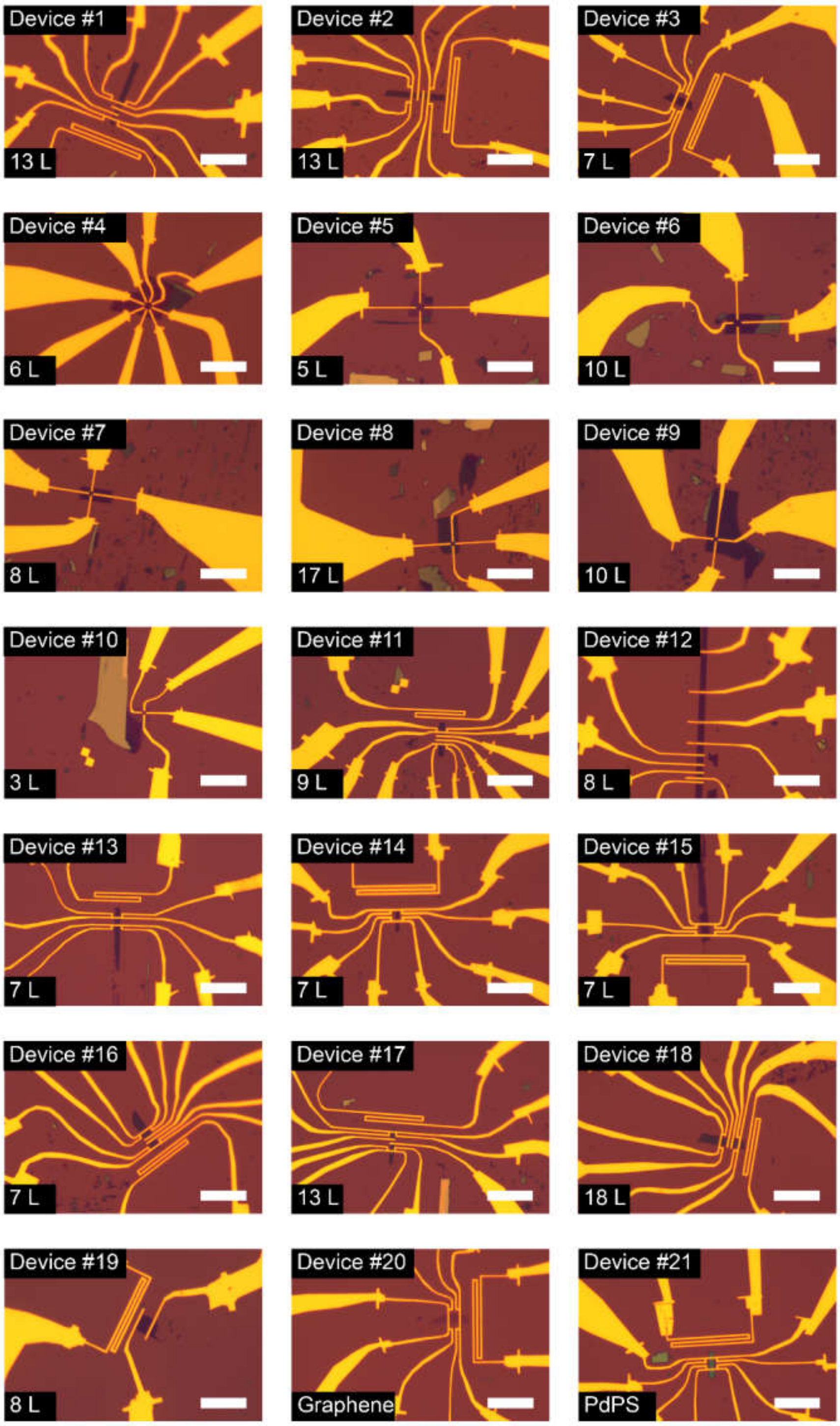

Supplementary Figure 17. Optical image of the measurement devices. Optical image of Device #1 to #21. The scale bar is 20 μm.

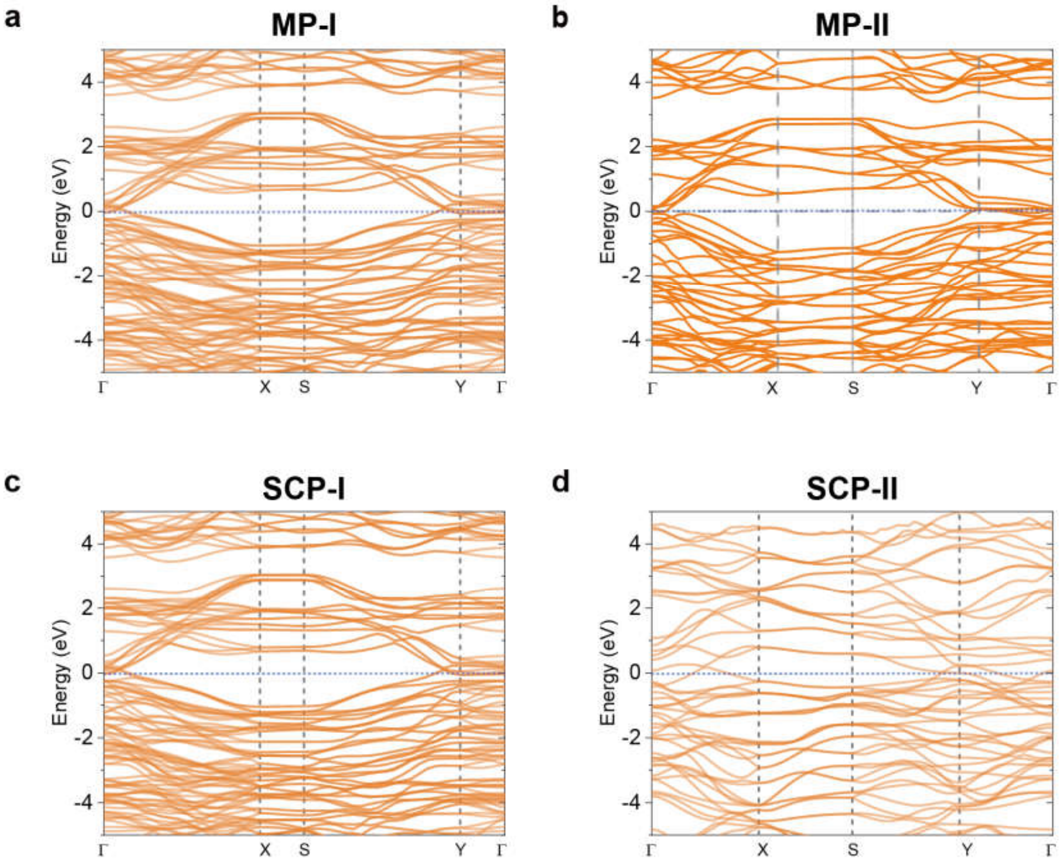

Supplementary Figure 18 Band structure of TNS under different phases obtained by first-principle calculations. a-d Band structure of TNS for metal phase I (**a**), metal phase II (**b**), correlated phase I (**c**), correlated phase II (**d**) obtained by first-principle calculations.

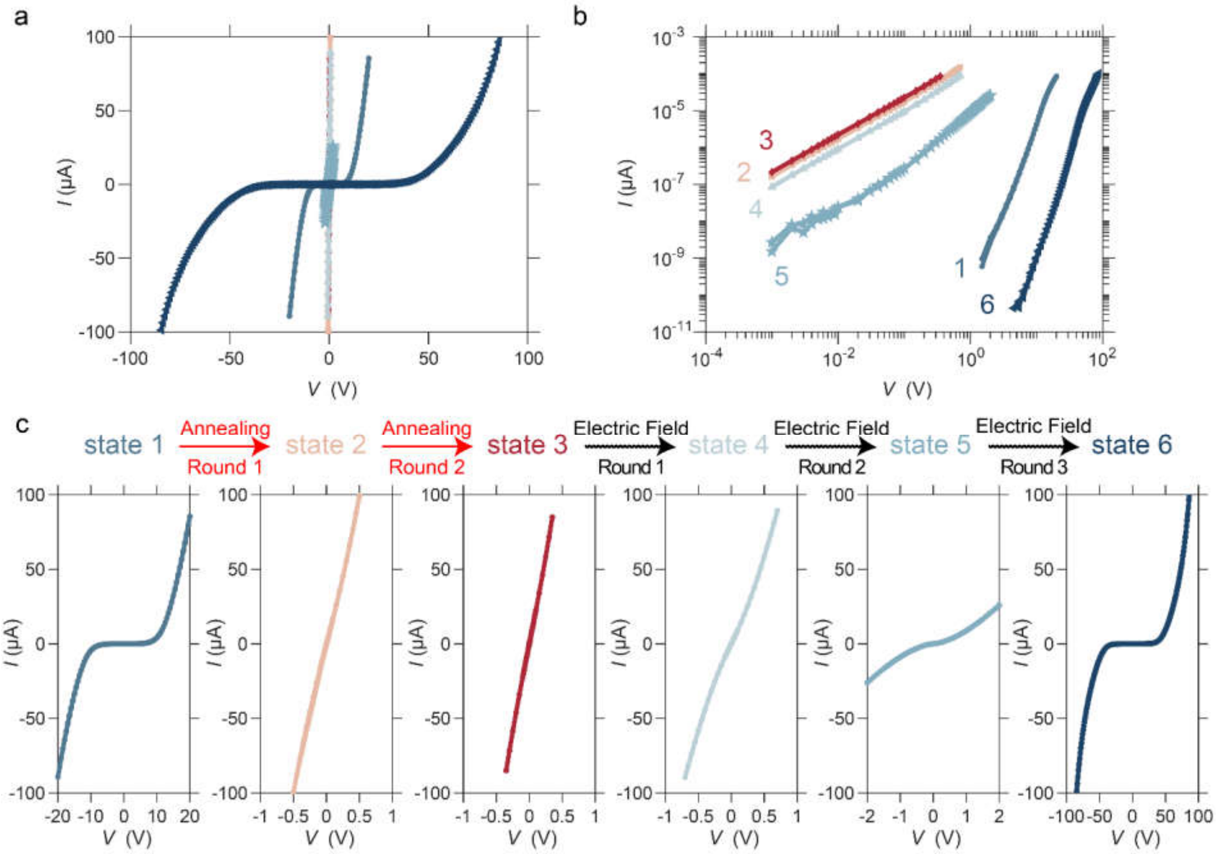

Supplementary Figure 19. Cyclic multistage phase transition in Device #2. a,b An overall demonstration of complete process of cyclic multistage phase transition plotted under normal (**a**) and logarithmic axes (**b**). **c** A step-by-step demonstration of complete process of cyclic multistage phase transition. All annealing operations are performed out at 500 K, while AC electric field operations are performed at 15K.

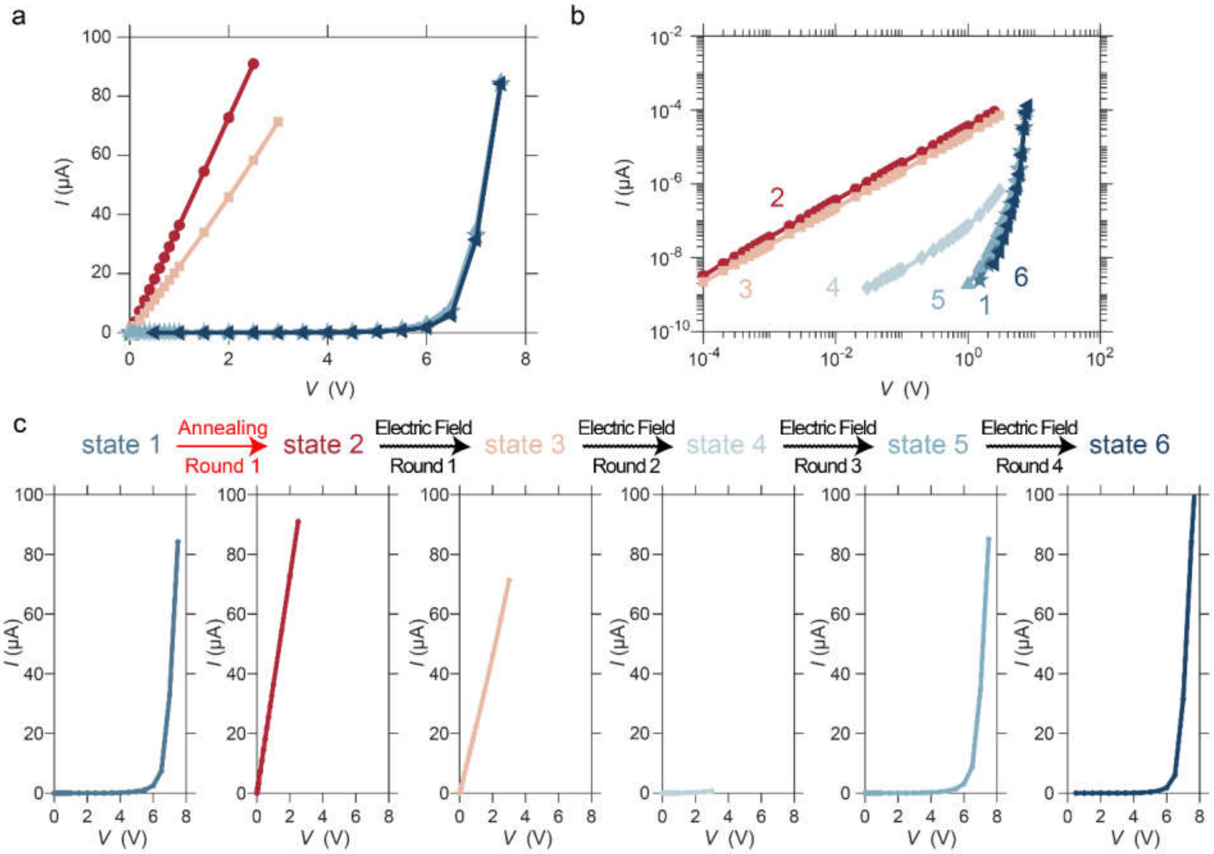

Supplementary Figure 20. Cyclic multistage phase transition in Device #3. a,b An overall demonstration of complete process of cyclic multistage phase transition plotted under normal (**a**) and logarithmic axes (**b**). **c** A step-by-step demonstration of complete process of cyclic multistage phase transition. All annealing operations are performed out at 500 K, while AC electric field operations are performed at 15K.

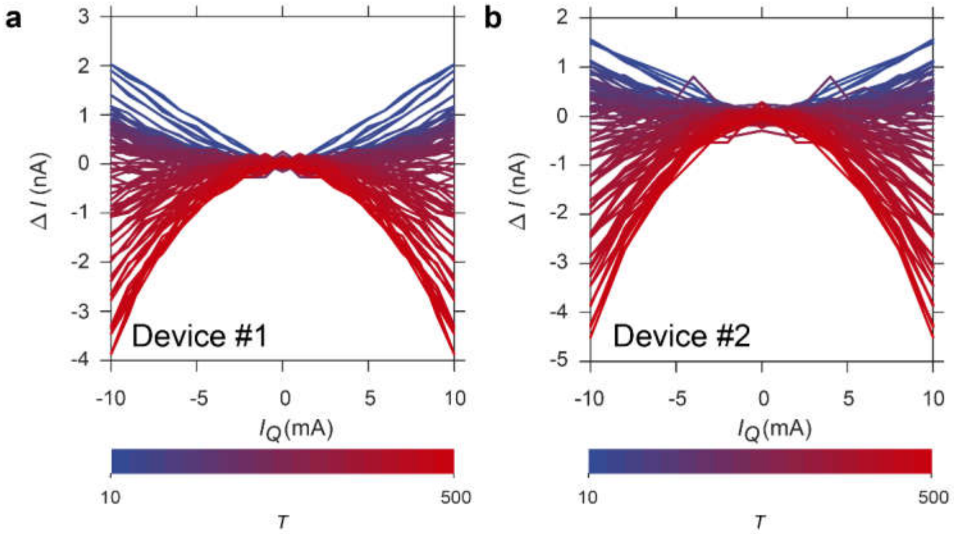

Supplementary Figure 21. Original data of TIC measurement under different temperatures. a,b Original data of TIC measurement in Device #1 (**a**) and #2 (**b**) under different temperatures.

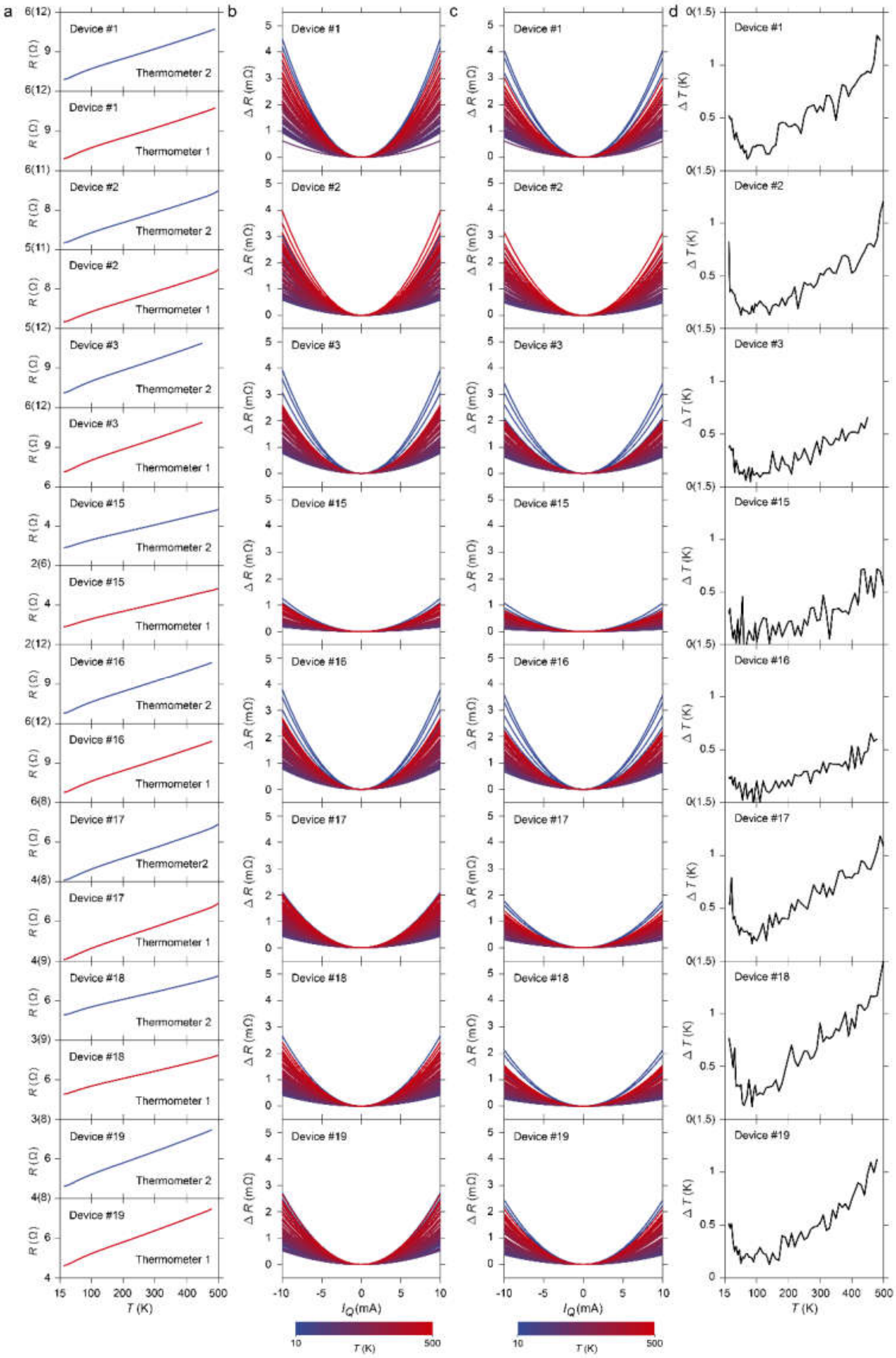

Supplementary Figure 22. Temperature difference in TIC measurement under different temperatures. a Temperature dependent resistance of thermometers in different devices. **b,c** Resistance change of thermometers in different devices under different temperature. **d** The measured temperature difference of two thermometers in different devices as a function of temperature.

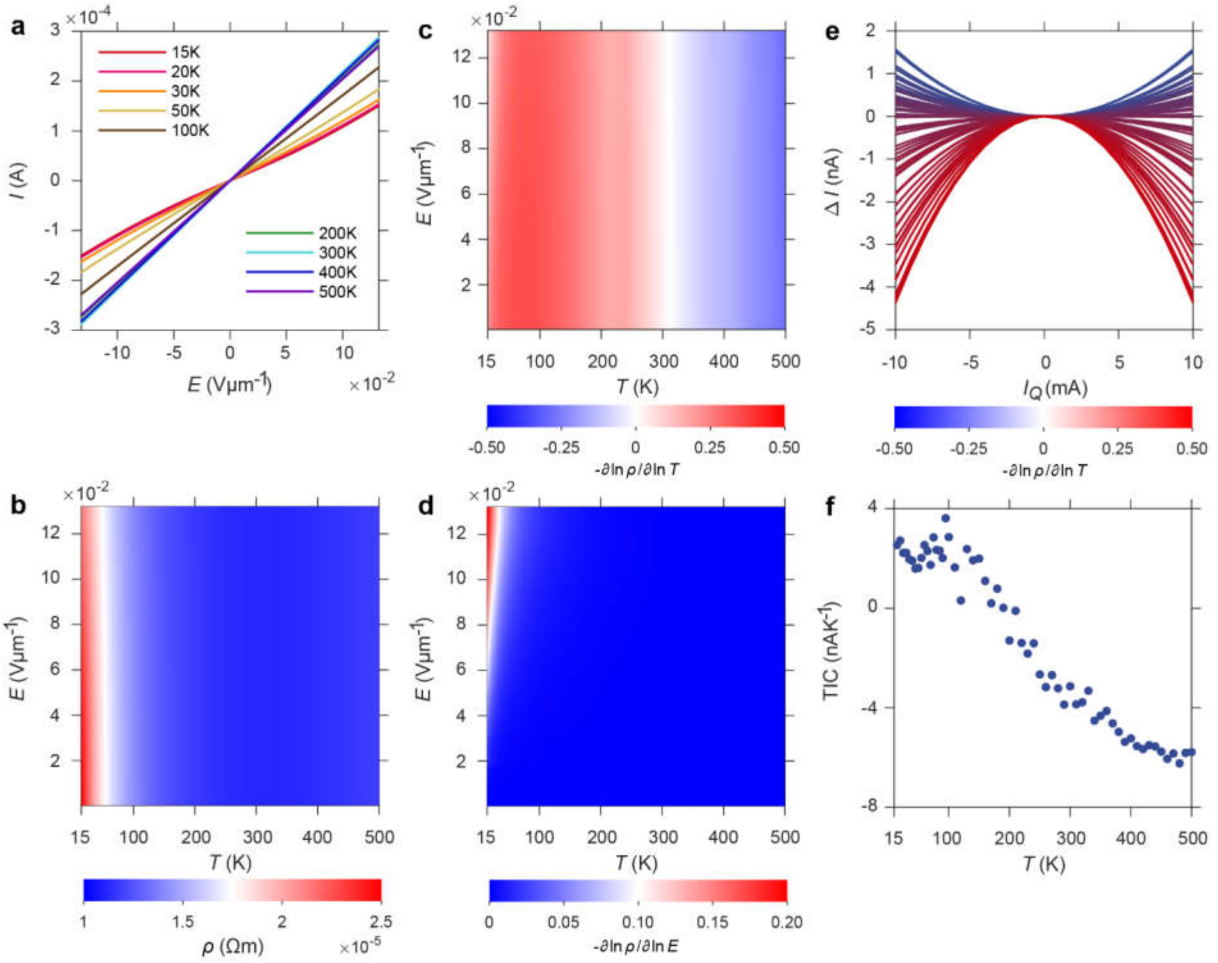

Supplementary Figure 23. Transport characterization along *a*-axis of phase II in Device #2. a,b Elcctric-field-current characteristic curves (**a**) and contour color map of resistivity (**b**) of phase II in Device #2. **c,d** Contour color map of temperature dependent (**c**) and electric-field dependent (**d**) carrier activation energy of phase II in Device #2. **e** TIC characteristic curves under different temperatures. **f** TIC of phase II under different temperatures in Device #2.

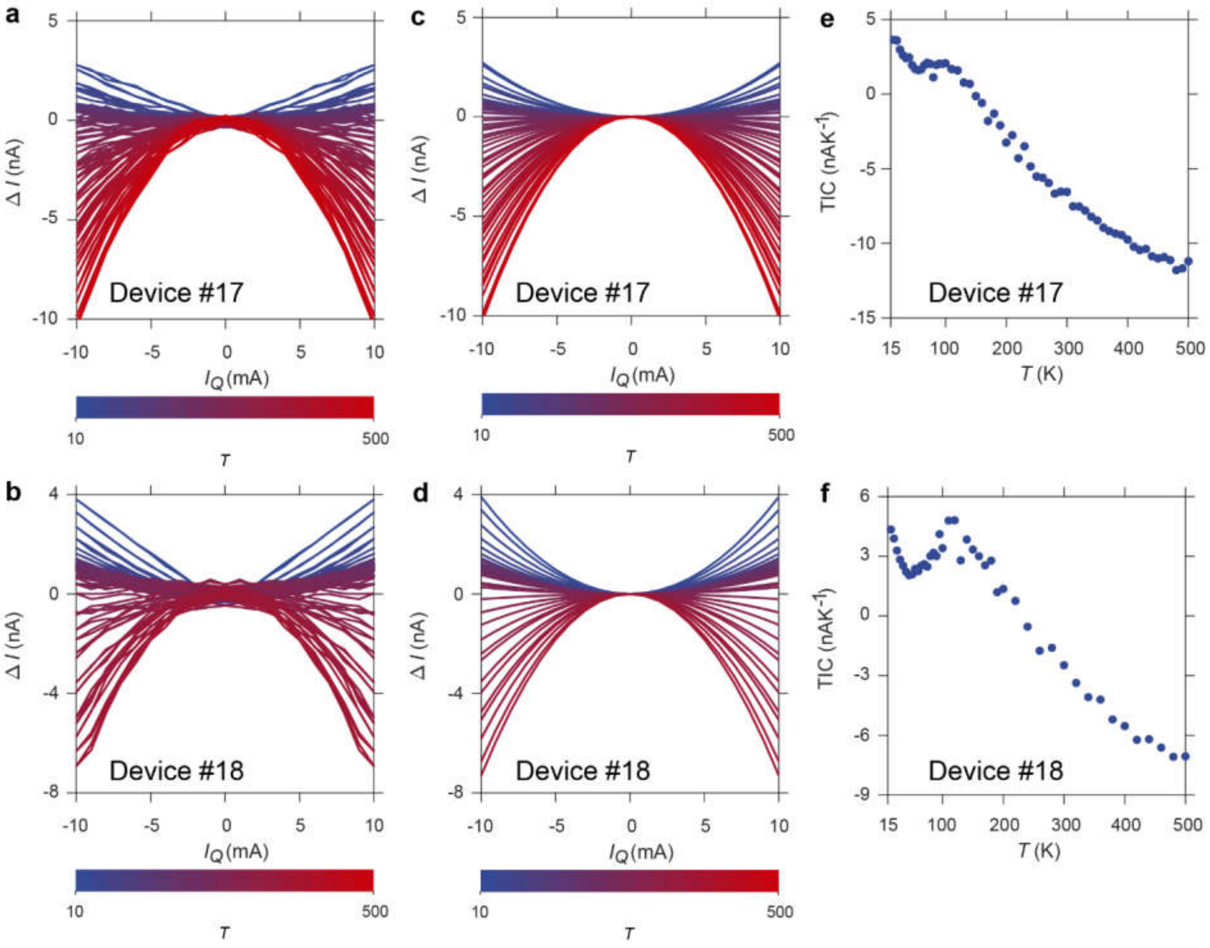

Supplementary Figure 24. TIC measurement in Device #17 and #18. a-d Original measurement results (**a**,**b**) and corresponding parabolic fitting results (**c**,**d**) of TIC in Device #17 (**a**,**c**) and #18 (**b**,**d**). **e**,**f** TIC in Device #17 (**e**) and #18 (**f**).

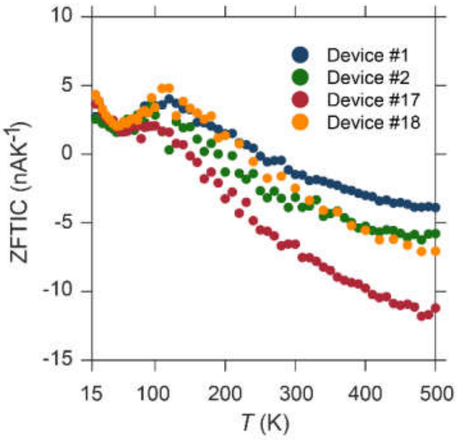

Supplementary Figure 25. The summarized TIC in different devices. TIC in Device #1 (blue dot), Device #2 (green dot), Device #17 (red dot) and #18 (orange dot).

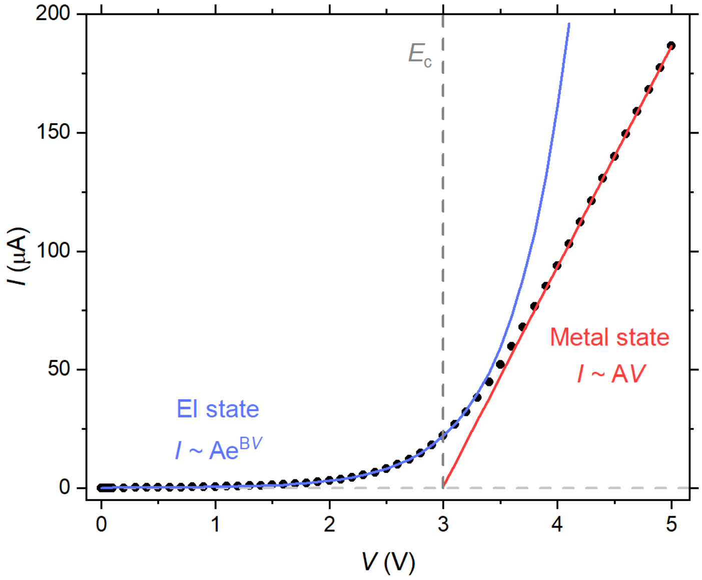

Supplementary Figure 26. A basic fitting of the electric-field-current curve in correlated phase II of TNS flake.

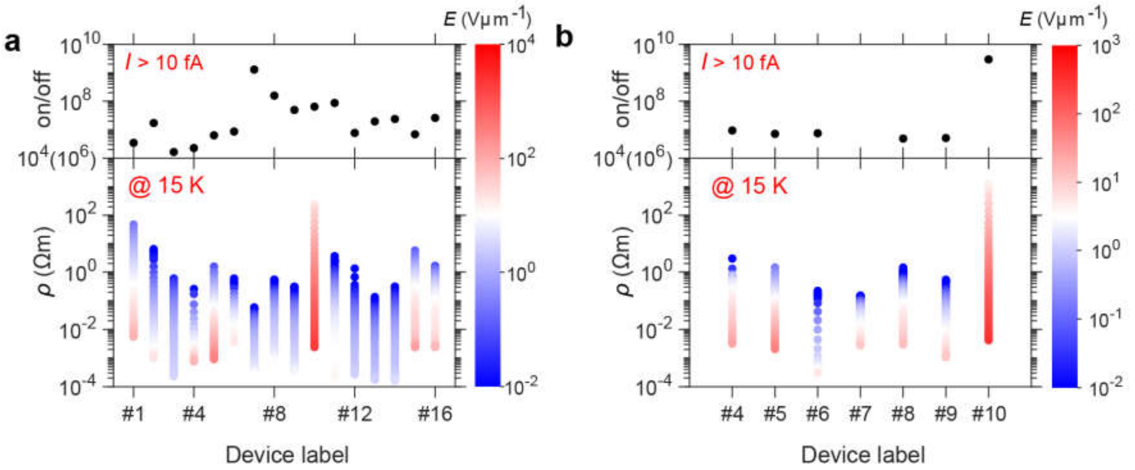

Supplementary Figure 27. Electric-field dependent resistivity and on-off ratio in different devices.

a,b Electric-field dependent resistivity and on-off ratio along ***a***-axis (**a**) and ***b***-axis (**b**) at 15 K.

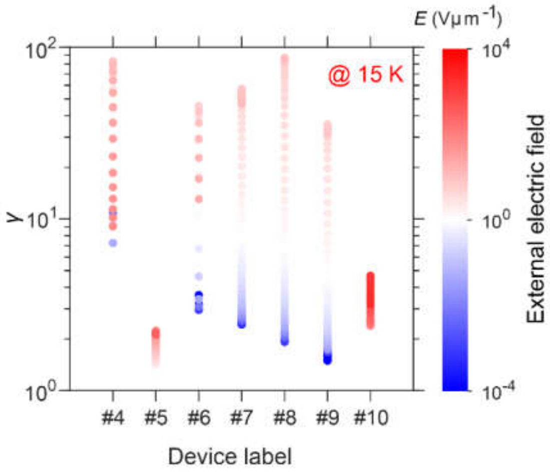

Supplementary Figure 28. Electric-field dependent electronic transport anisotropy in different devices.

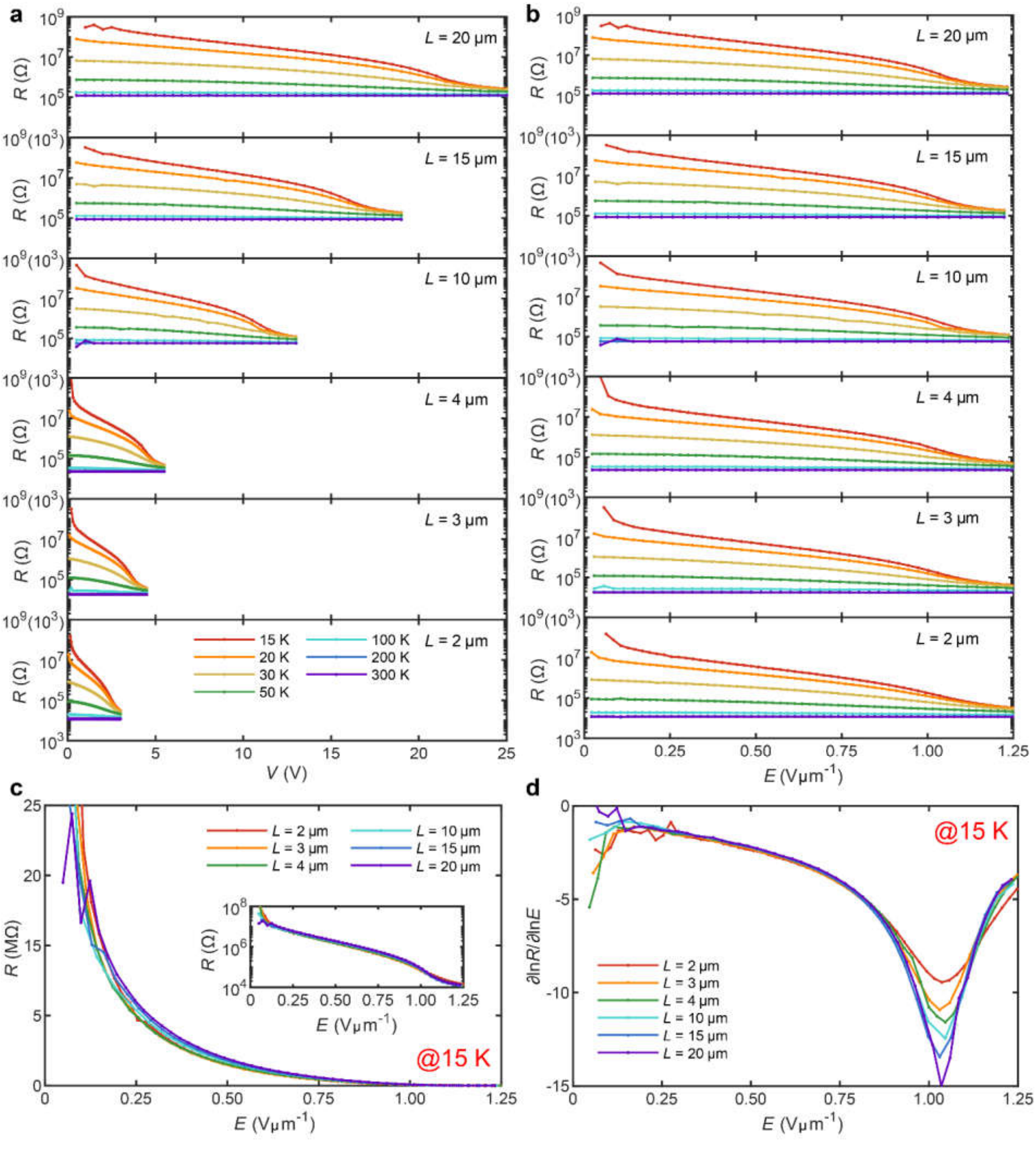

Supplementary Figure 29. Length independent transport characterization of phase I in Device #12. **a,b** Electric-voltage (**a**) and electric-field (**b**) dependent resistance of phase I in Device #12 under different temperatures.**c,d** Length independent resistance (**c**) and its first derivative (**d**) of phase I in Device #12.

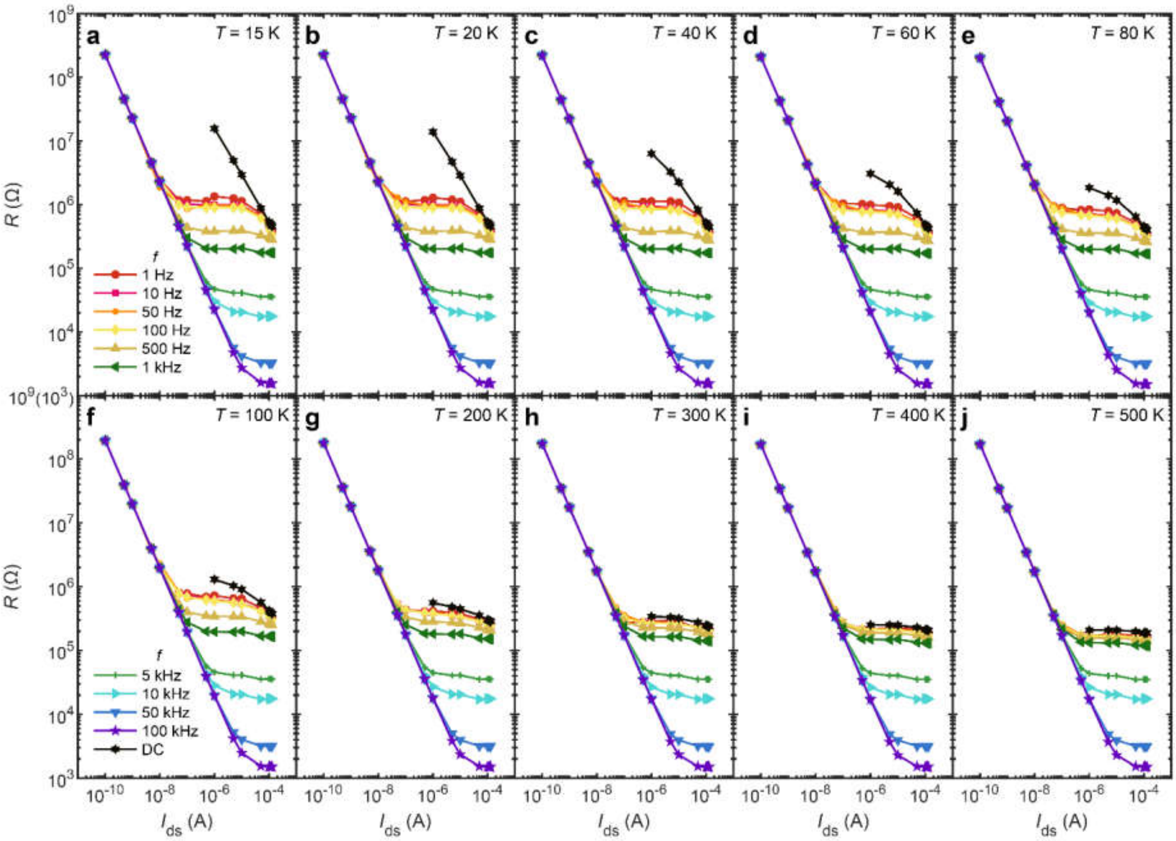

Supplementary Figure 30. AC transport characterization of phase I in Device #5. a-j AC transport characterization of phaseI in Device #5 under the temperature range from 15 K to 500 K.

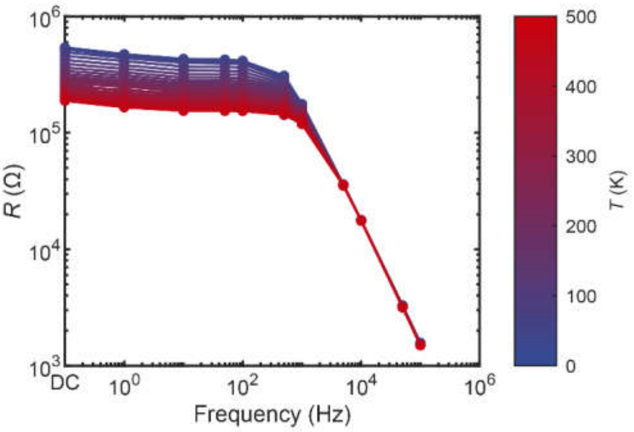

243

244 **Supplementary Figure 31. Frequency dependent AC transport characterization of phase I in Device**

245 **#5.**

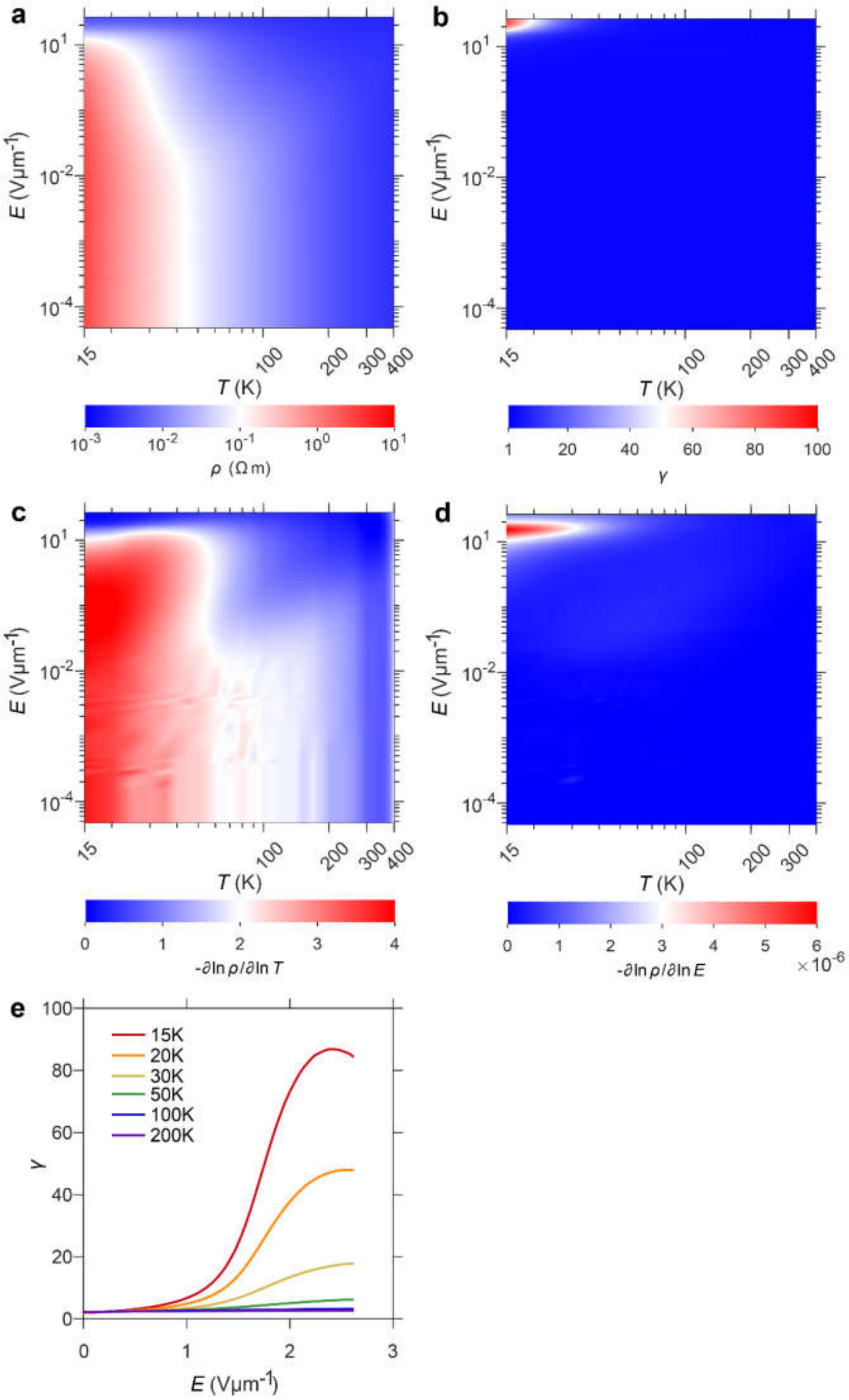

Supplementary Figure 32. Transport characterization of phase I in Device #8. a Contour color map of resistivity along ***b***-axis of phase I in Device #8. **b** Contour color map of electronic transport anisotropy of phase I in Device #8. **c-d** Contour color map of temperature dependent (**c**) and electric-field dependent (**d**) carrier activation energy along ***b***-axis of phase I in Device #8. **e** Electronic transport anisotropy of phase I in Device #8.

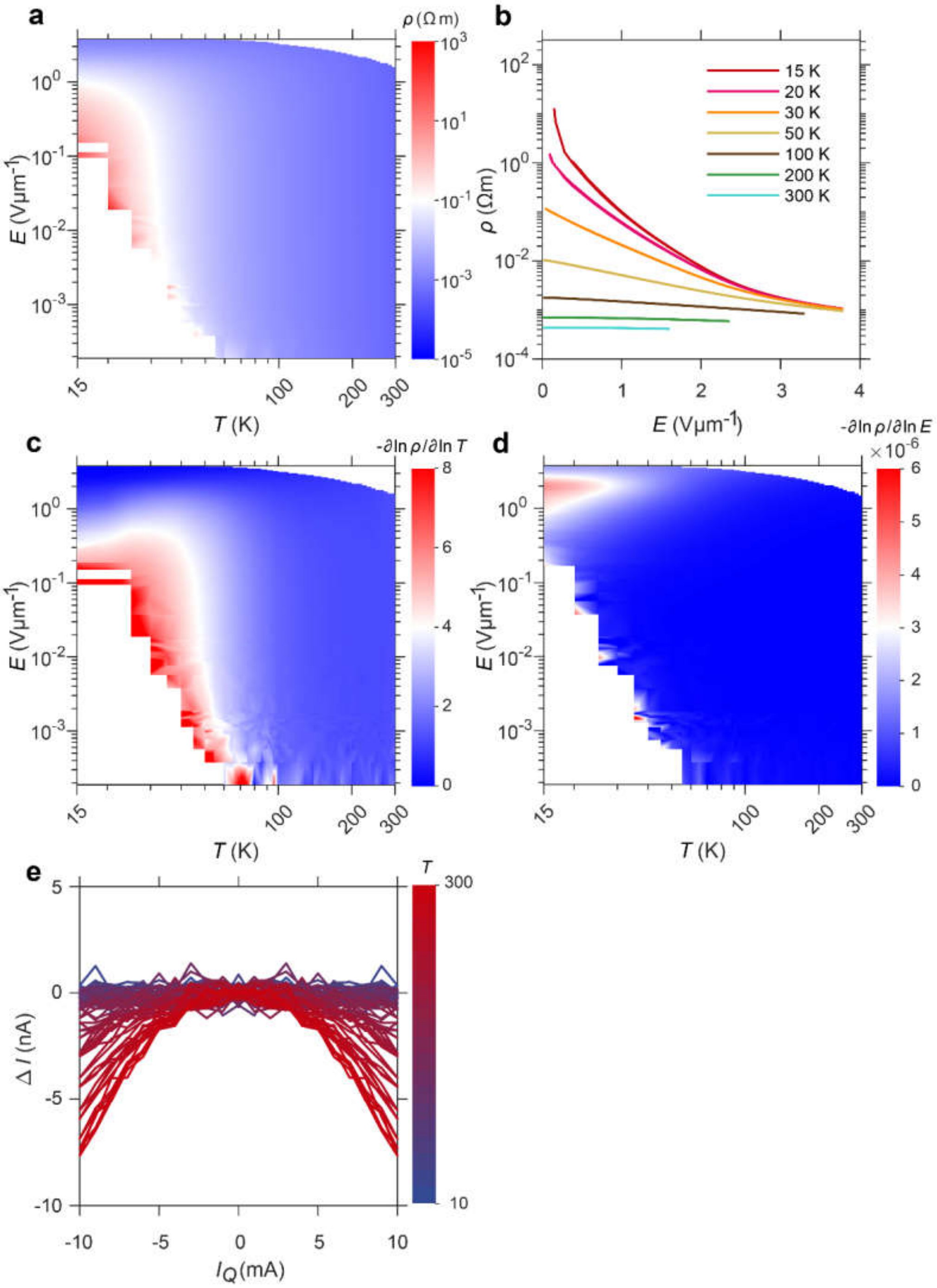

Supplementary Figure 33. Transport characterization of phase I in Device #1. a Contour color map of resistivity along ***a***-axis of phase I in Device #1. **b** Temperature dependent electric-field-current characteristic curves of phase I in Device #1. **c-d** Contour color map of temperature dependent (**c**) and electric-field dependent (**d**) carrier activation energy along ***a***-axis of phase I in Device #1. **e** Original measurement results ofTIC along ***a***-axis measured in Device #1.

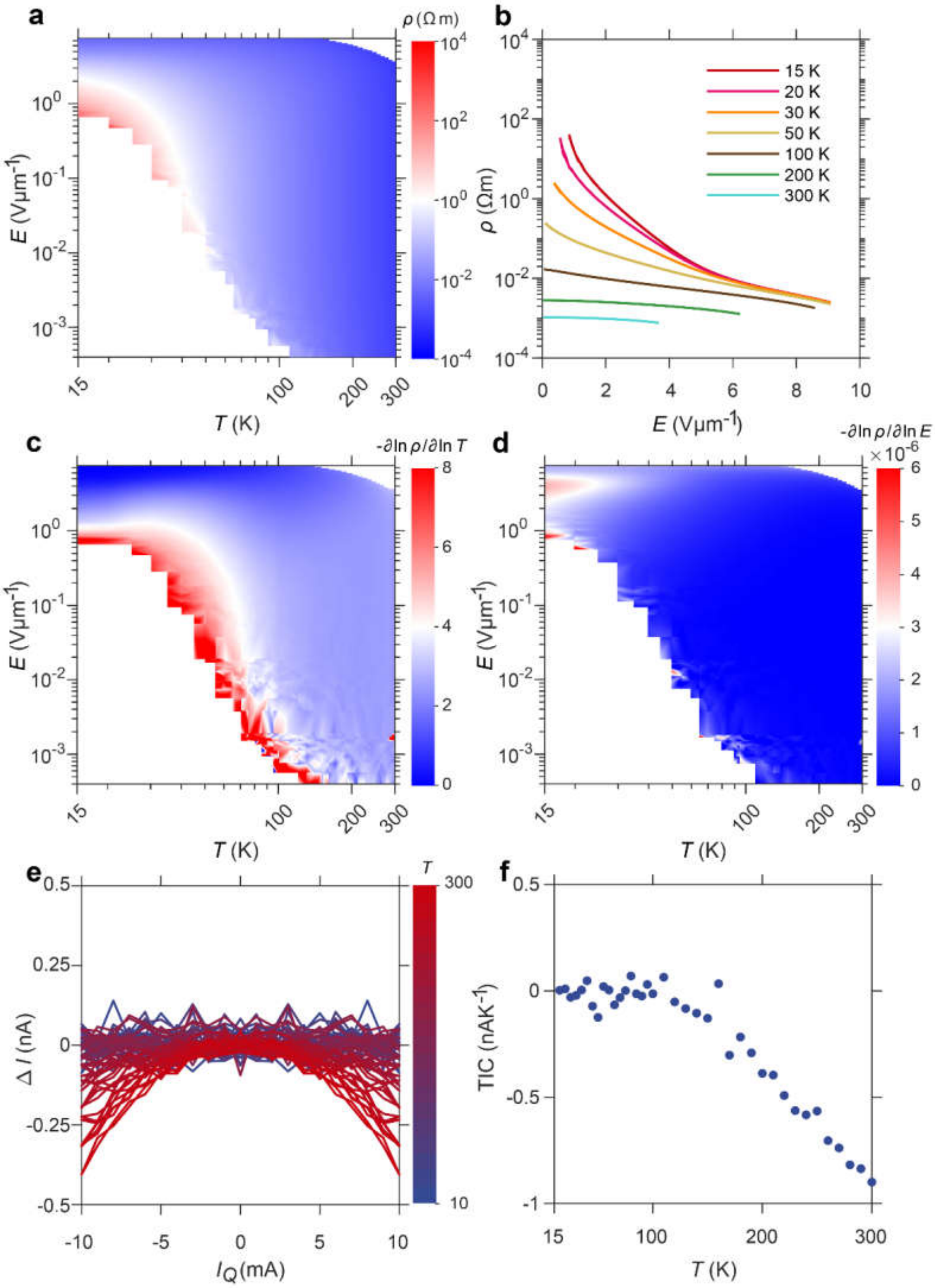

Supplementary Figure 34. Transport characterization of phase I in Device #2. a Contour color map of resistivity along ***a***-axis of phase I in Device #2. **b** Temperature dependent electric-field-current characteristic curves of phase I in Device #2. **c-d** Contour color map of temperature dependent (**c**) and electric-field dependent (**d**) carrier activation energy along ***a***-axis of phase I in Device #2. **e** Original measurement results of TIC along ***a***-axis measured in Device #2. **f** TIC along ***a***-axis of phase I in Device #2.

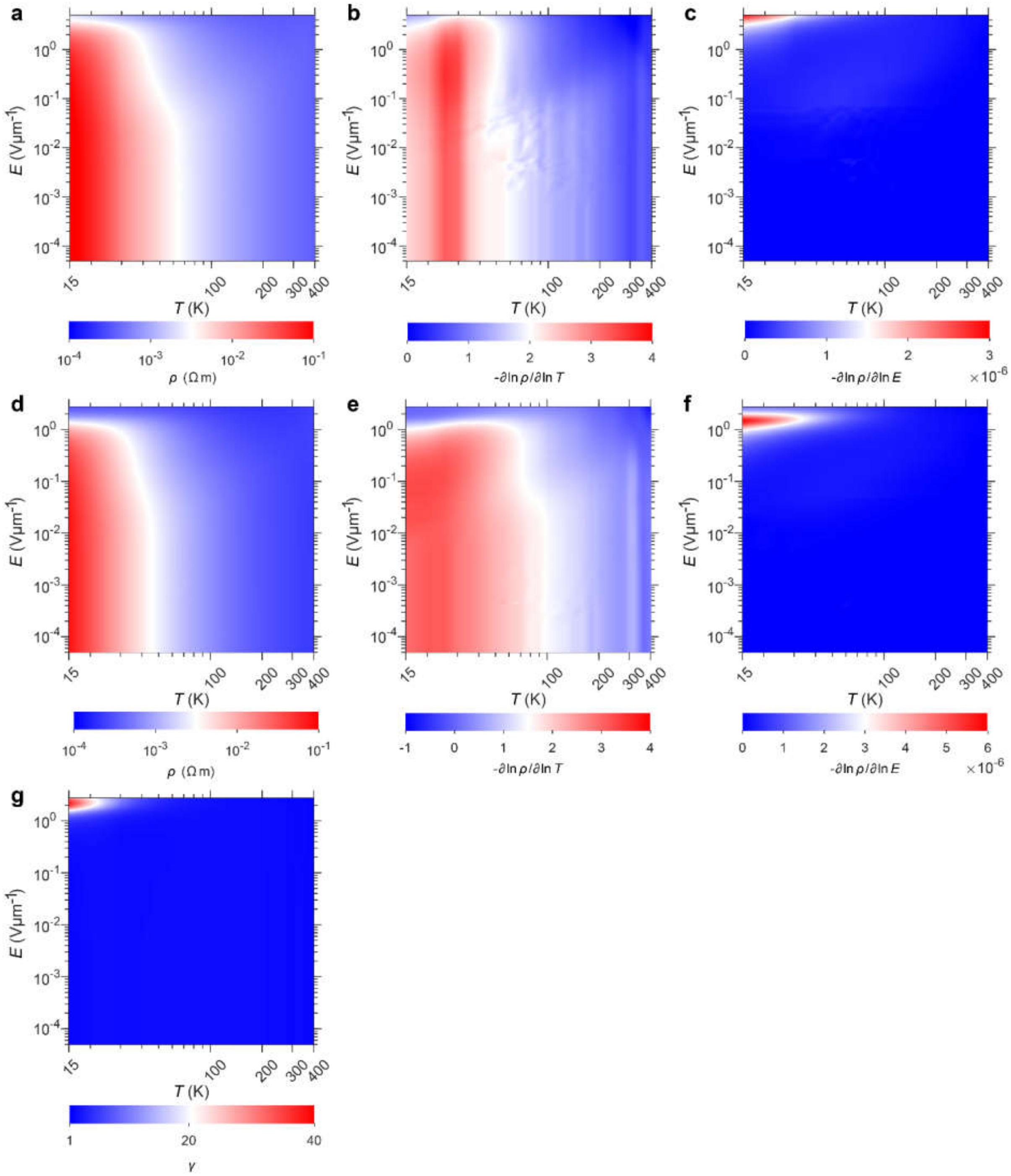

Supplementary Figure 35. Transport characterization of phase I in Device #7. a-c Contour color map of resistivity (**a**), temperature dependent (**b**) and electric-field dependent (**c**) carrier activation energy along ***a***-axis of phase I in Device #7. **d-f** Contour color map of resistivity (**d**), temperature dependent (**e**) and

electric-field dependent (**f**) carrier activation energy along ***b***-axis of phase I in Device #7. **g** Contour color map of electronic transport anisotropy of phase I in Device #7.

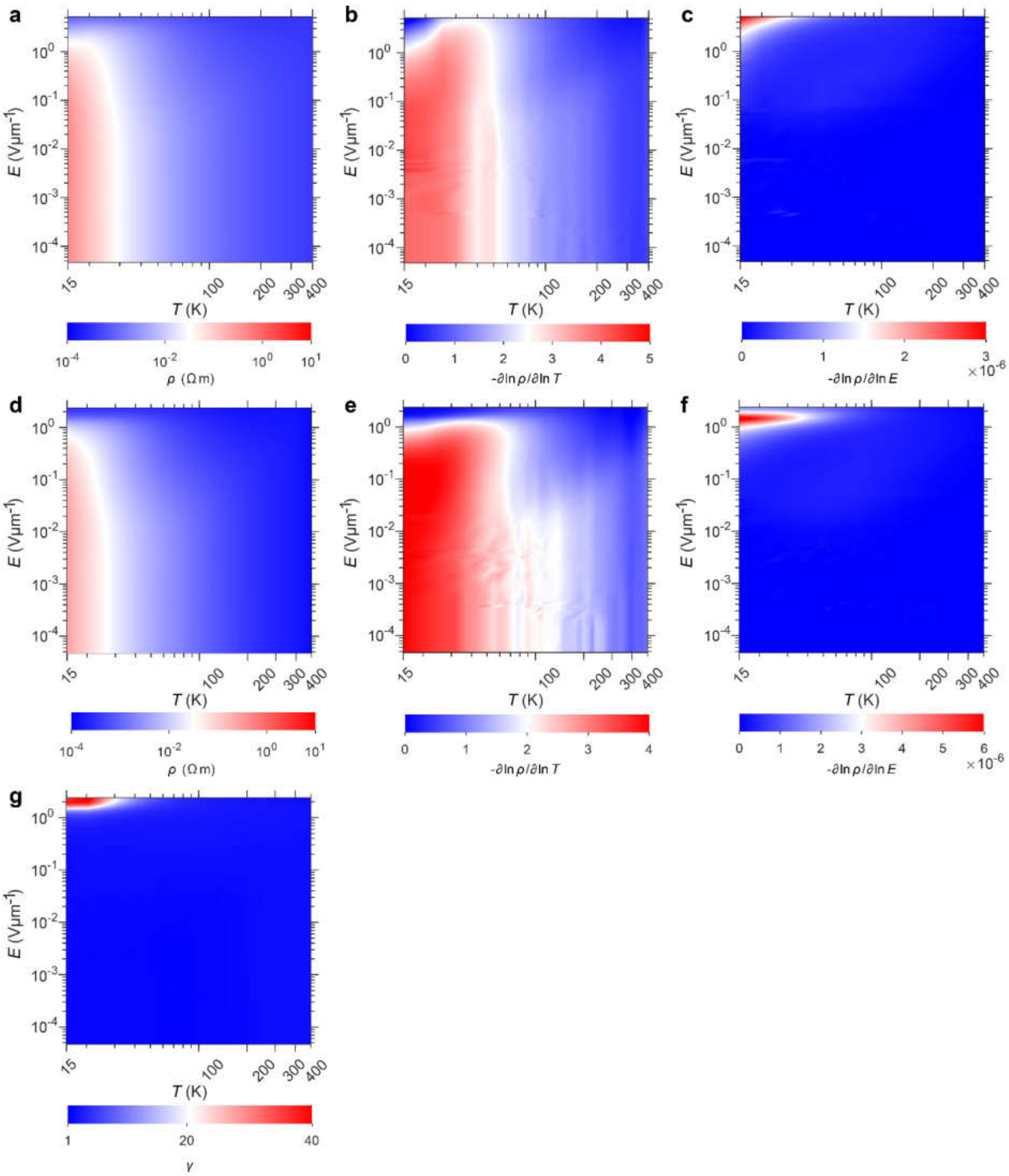

Supplementary Figure 36. Transport characterization of phase I in Device #9. a-c Contour color map of resistivity (**a**), temperature dependent (**b**) and electric-field dependent (**c**) carrier activation energy along ***a***-axis of phase I in Device #9. **d-f** Contour color map of resistivity (**d**), temperature dependent (**e**) and

electric-field dependent (**f**) carrier activation energy along ***b***-axis of phase I in Device #9. **g** Contour color map of electronic transport anisotropy of phase I in Device #9.

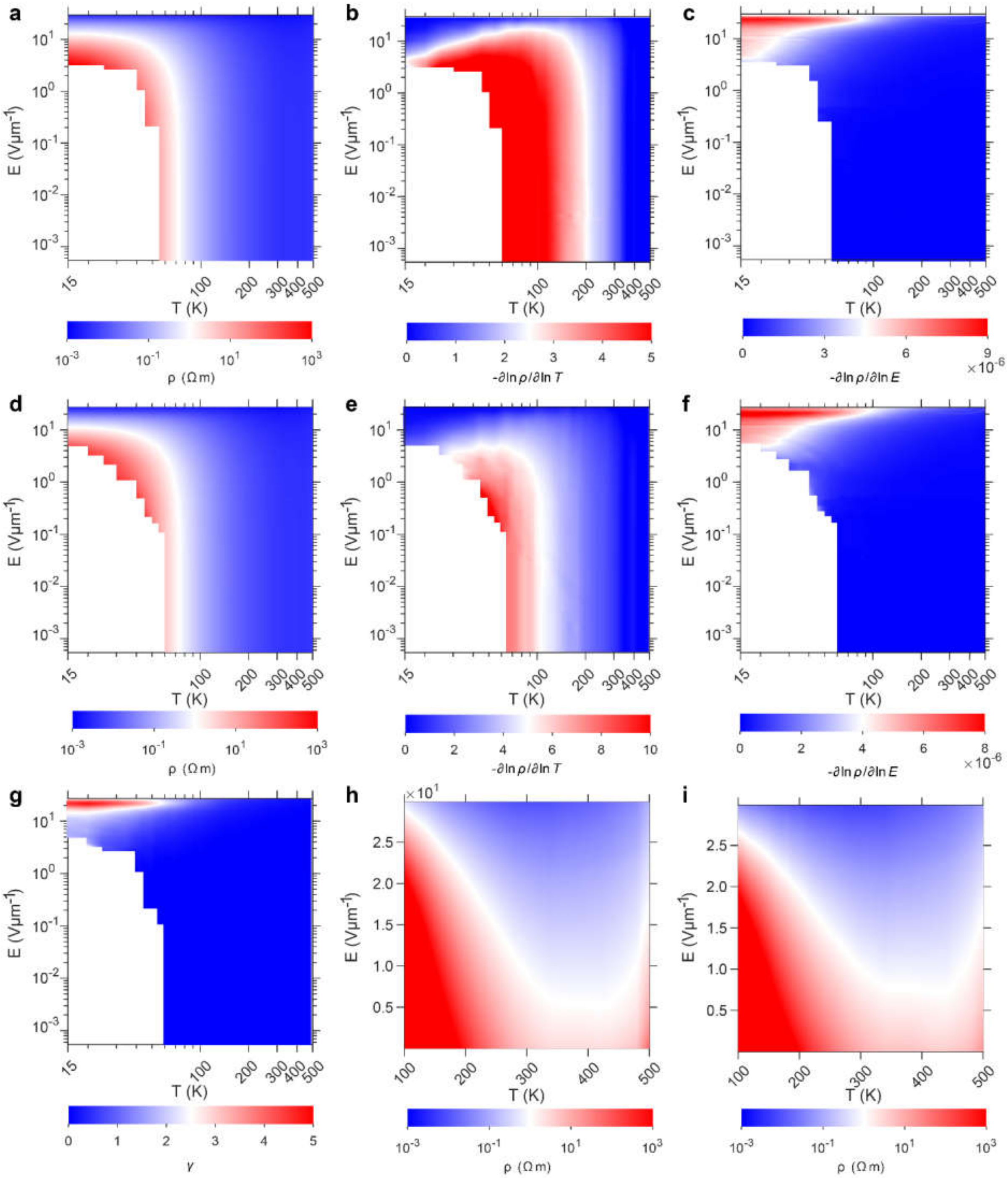

Supplementary Figure 37. Transport characterization of phase I in Device #10. a-c Contour color map of resistivity (**a**), temperature dependent (**b**) and electric-field dependent (**c**) carrier activation energy along ***a***-axis of phase I in Device #10. **d-f** Contour color map of resistivity (**d**), temperature dependent (**e**) and

electric-field dependent (**f**) carrier activation energy along ***b***-axis of phase I in Device #10. **g** Contour color map of electronic transport anisotropy of phase I in Device #10. **h**,**i** Amplified contour color map of resistivity along ***a***-axis (**h**) and ***b***-axis (**i**) of phase I in Device #10.

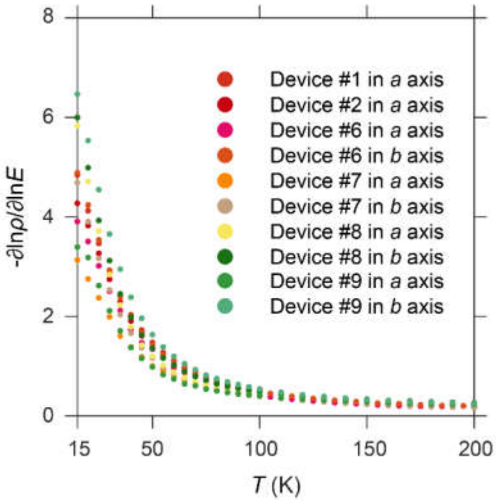

Supplementary Figure 38. Electric-field dependent carrier activation energy in different devices and axes.

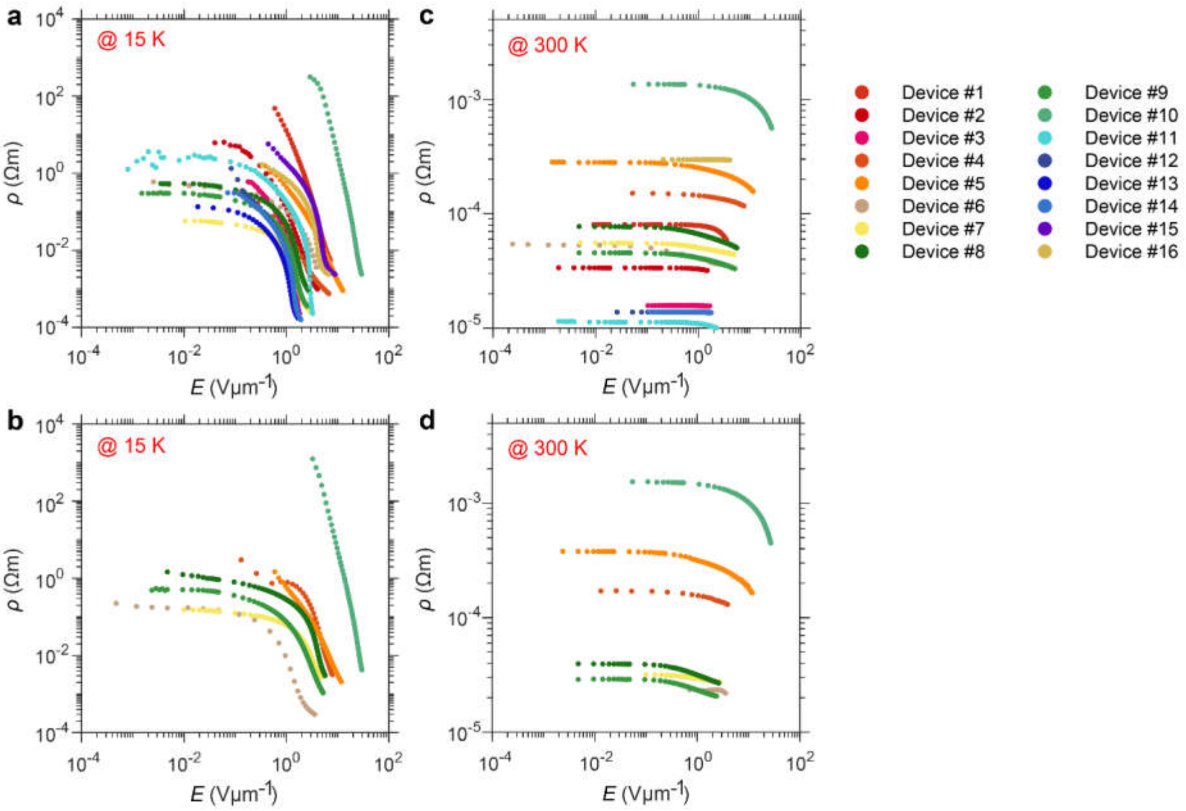

Supplementary Figure 39. Electric-field dependent resistivity in different devices and temperatures. **a,b** Electric-field dependent resistivity along ***a***-axis (**a**) and ***b***-axis (**b**) at 15 K. **c,d** Electric-field dependent resistivity along ***a***-axis (**a**) and ***b***-axis (**b**) at 300 K.

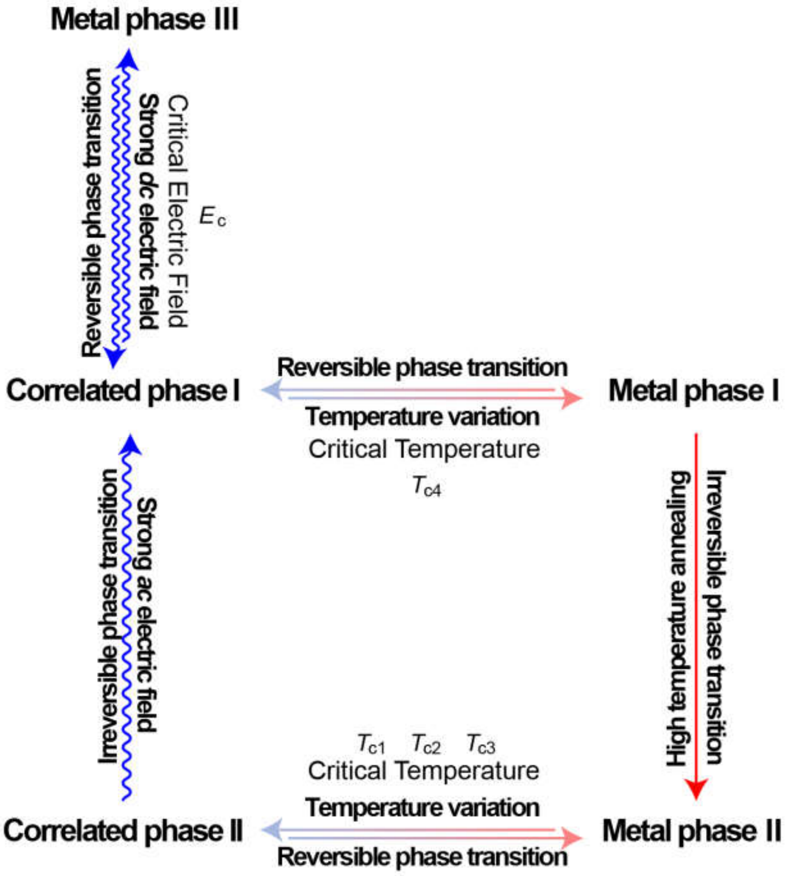

Supplementary Figure 40. Complete phase diagram and modulation method of few layer TNS.

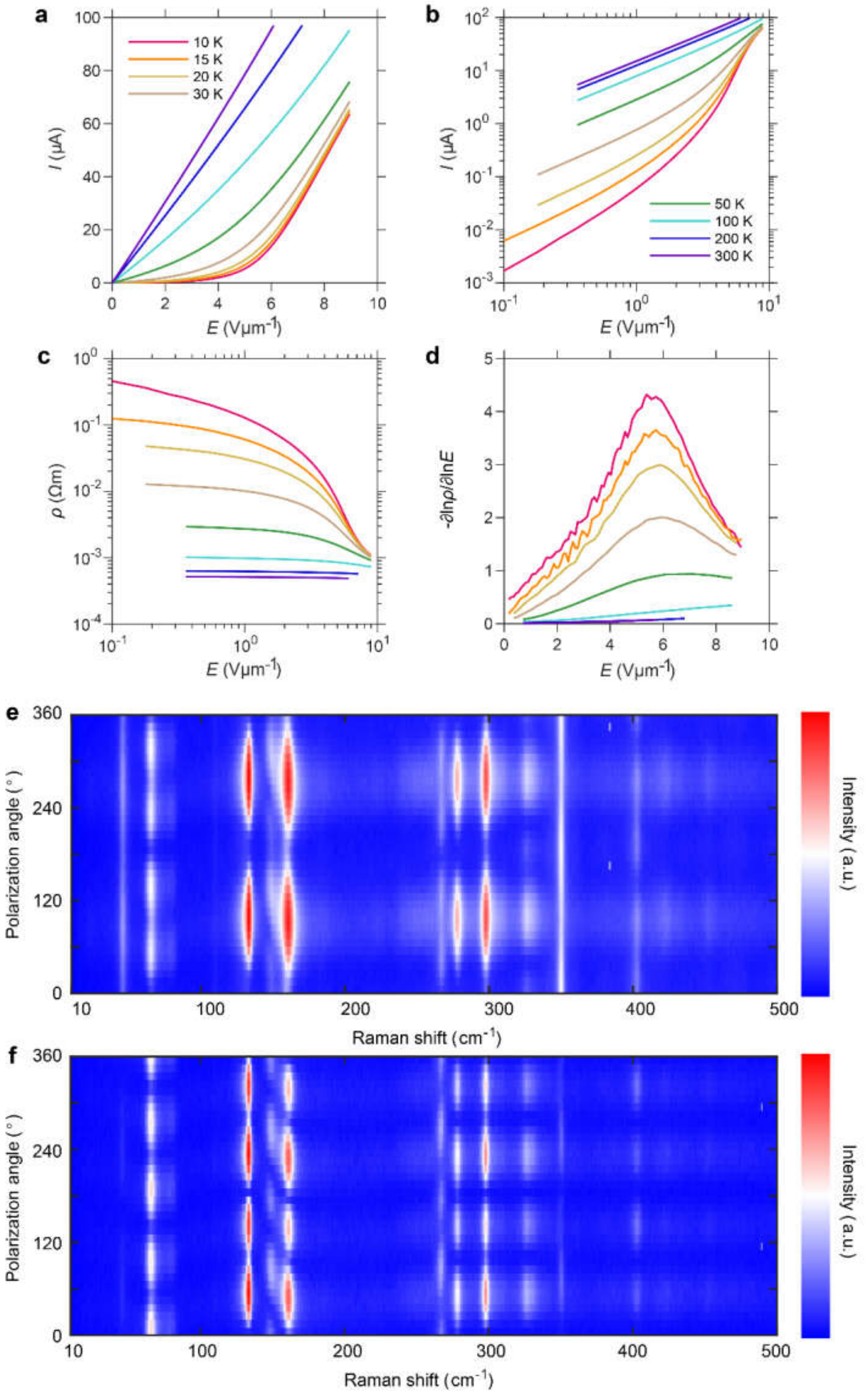

302

303 **Supplementary Figure 41. Transport characterization and ARPRS characterization of phase I in**

304 **Device #19. a,b** Electric-field-current characteristic curves of phase I in Device #19 under normal (**a**) and

logarithmic axes (**b**). **c**,**d** Electric-field dependent resistivity (**c**) and carrier activation energy (**d**) of phase I in Device #19. **e**,**f** Contour color map of the ARPRS under XX (**e**) and XY (**f**) configurations at 9.5 K.

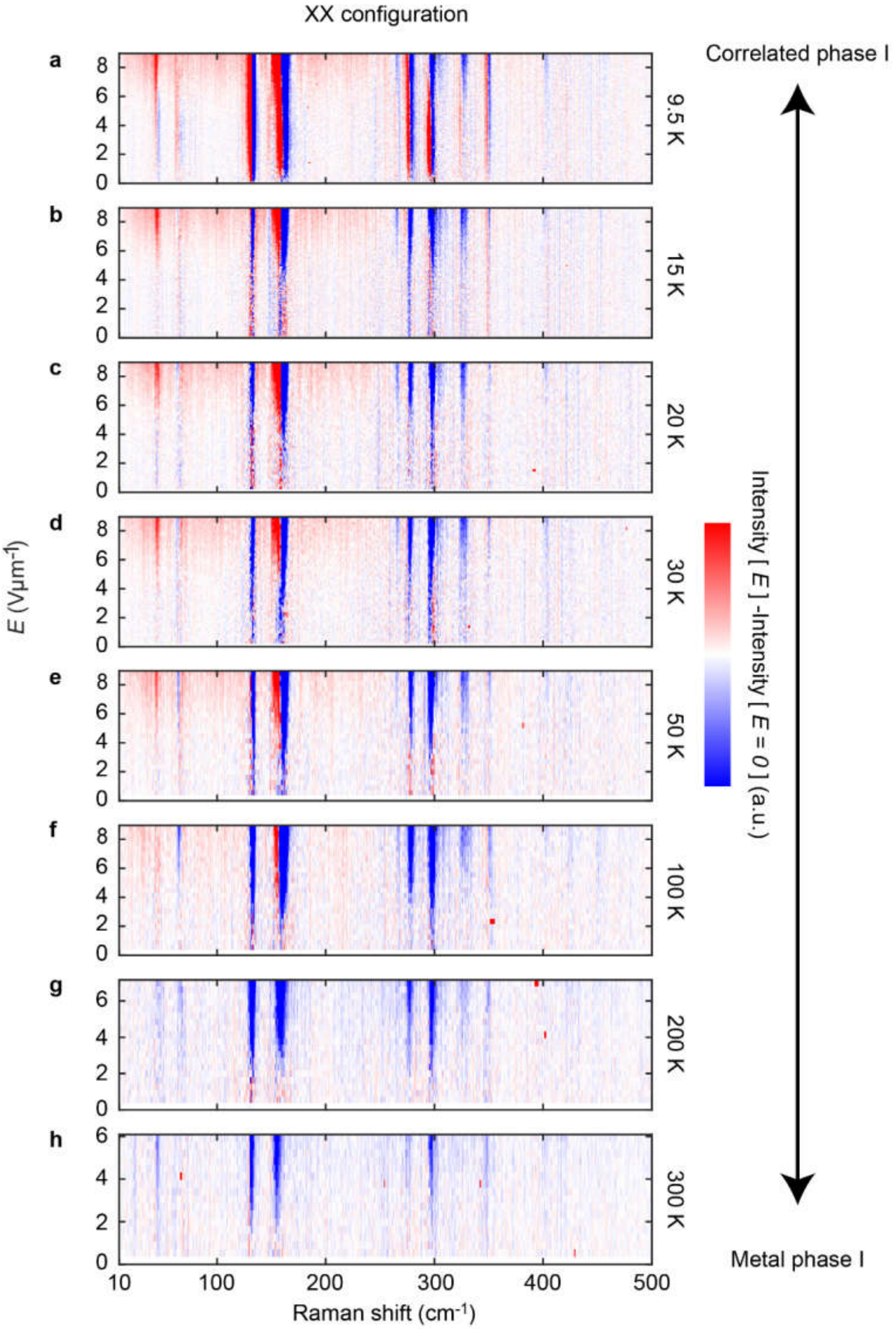

Supplementary Figure 42. Electric-field dependent polarized Raman spectroscopy characterization of phase I in Device #R3 under XX configuration. a-h Electric-field dependent polarized Raman spectroscopy for phase I in Device #R3 under XX configuration at 9.5 K, 15 K, 20 K, 30 K, 50 K, 100 K, 200 K, 300 K. Color represents the change induced by electric-field.

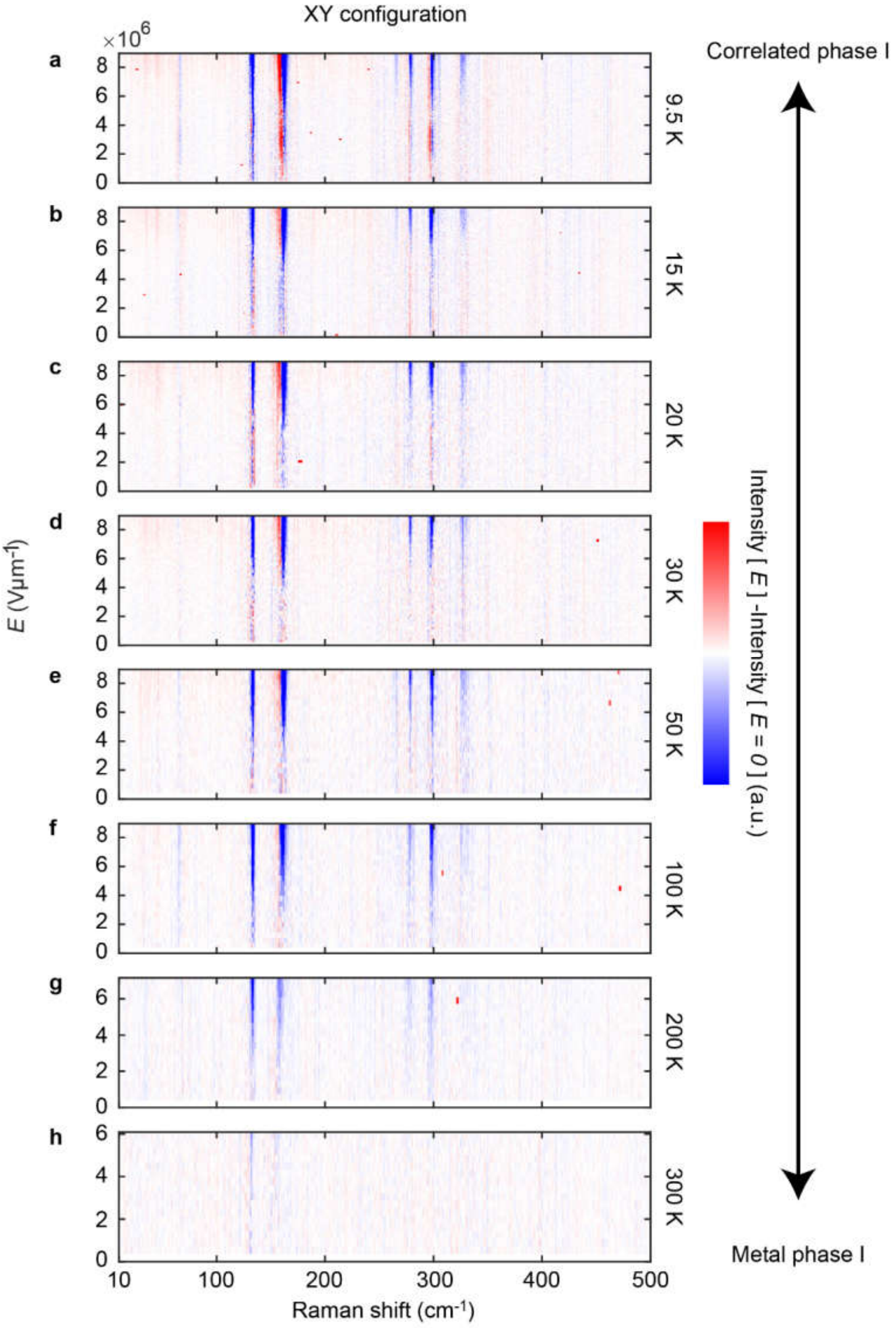

Supplementary Figure 43. Electric-field dependent polarized Raman spectroscopy characterization of phase I in Device #R3 under XY configuration. a-h Electric-field dependent polarized Raman spectroscopy for phase I in Device #R3 under XY configuration at 9.5 K, 15 K, 20 K, 30 K, 50 K, 100 K, 200 K, 300 K. Color represents the change induced by electric-field.

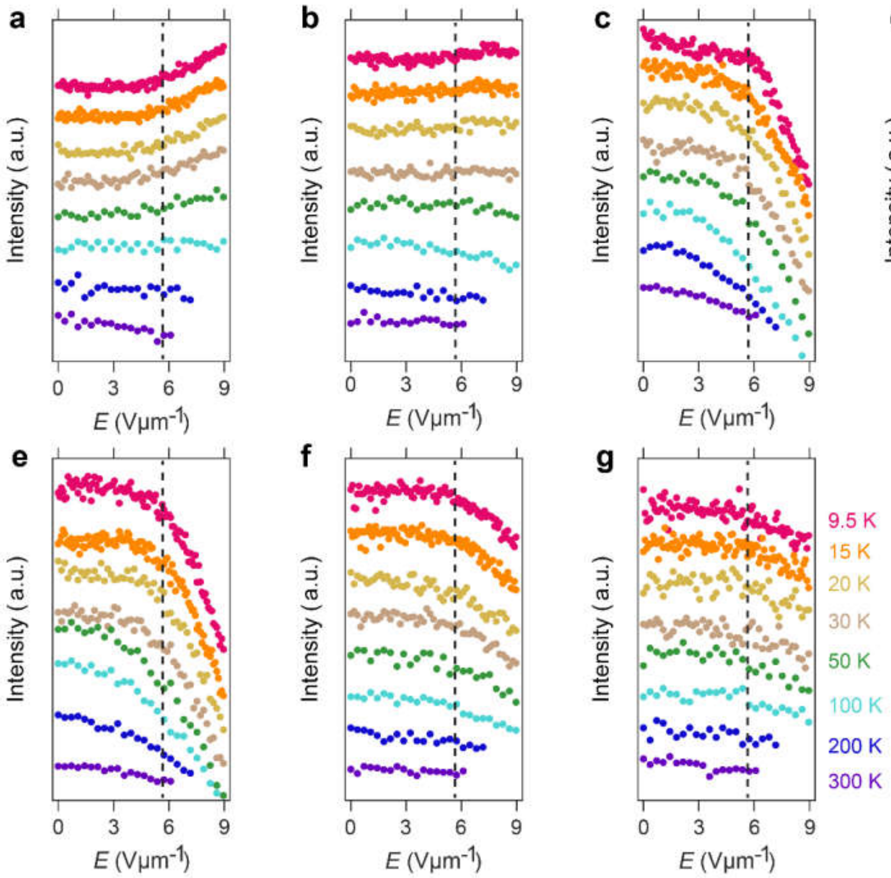

Supplementary Figure 44. Electric-field dependent intensity response of Raman characteristic peak of phase I in Device #R3 under XX configuration. a-g Electric-field dependent intensity response under XX configuration for Raman characteristic peak P_I^1, P_I^3, P_I^6, P_I^{11}, P_I^{12}, P_I^{14}, P_I^{17}.

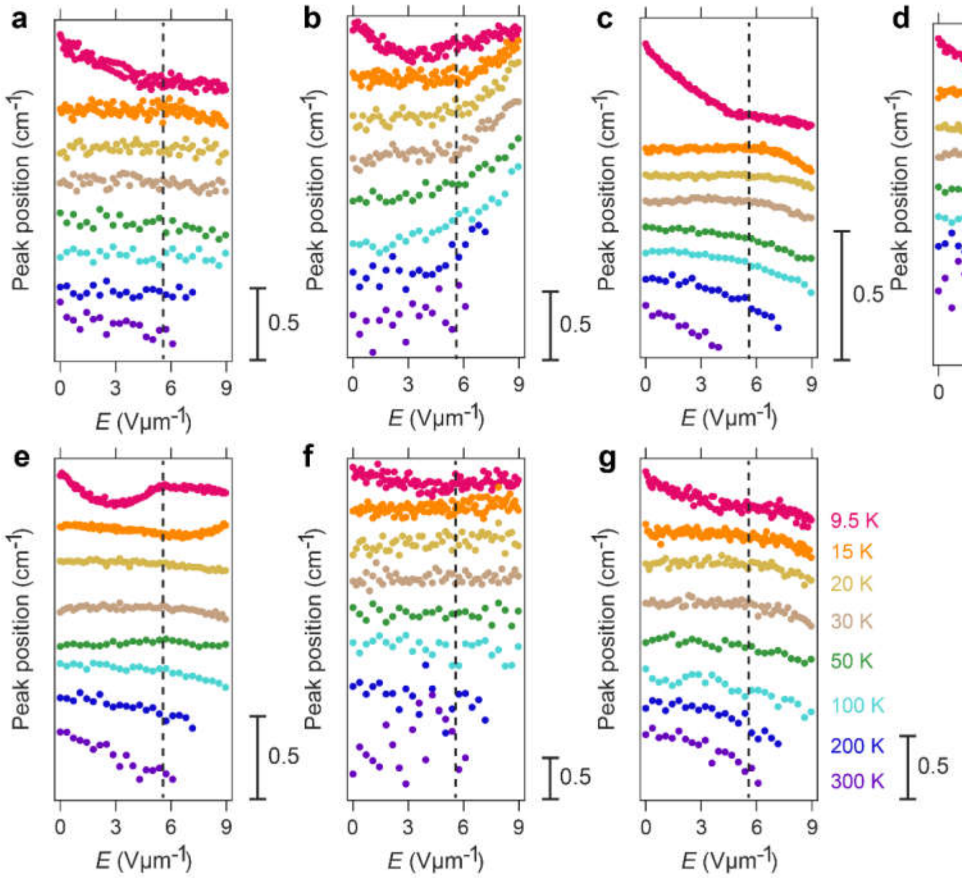

Supplementary Figure 45. Electric-field dependent peak position response of Raman characteristic peak of phase I in Device #R3 under XX configuration. a-g Electric-field dependent peak position response under XX configuration for Raman characteristic peak P_{I}^{1}, P_{I}^{3}, P_{I}^{6}, P_{I}^{11}, P_{I}^{12}, P_{I}^{14}, P_{I}^{17}.

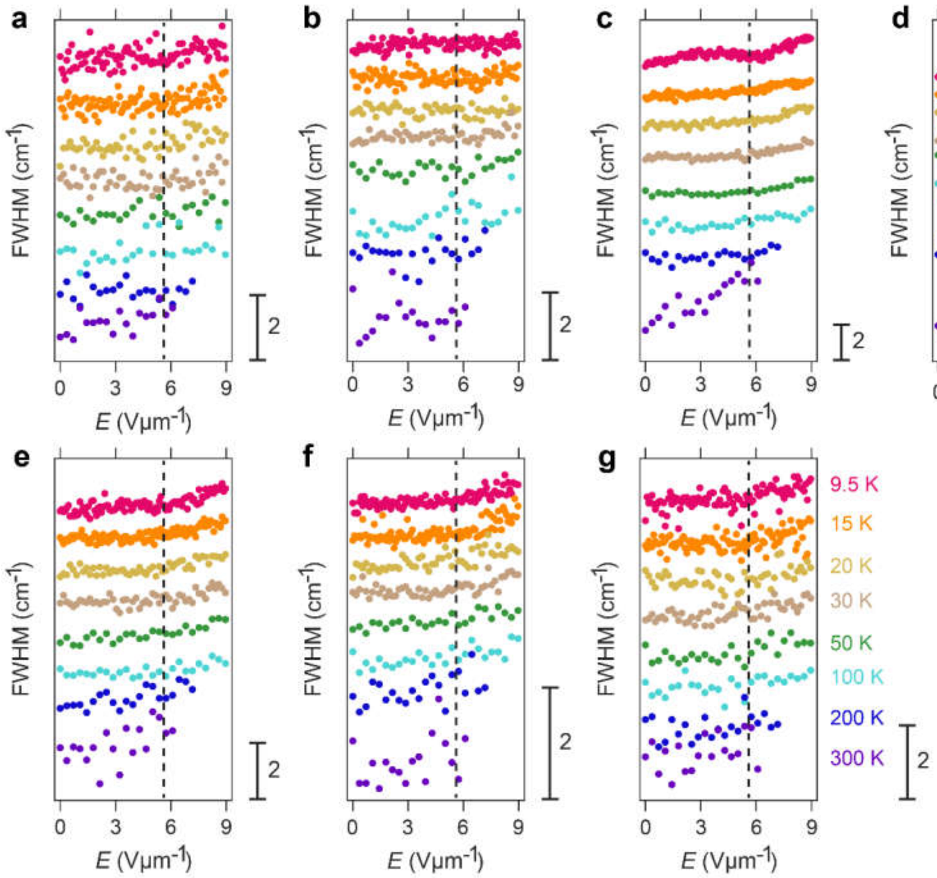

Supplementary Figure 46. Electric-field dependent full width at half maximum (FWHM) response of Raman characteristic peak of phase I in Device #R3 under XX configuration. a-g Electric-field dependent FWHM response under XX configuration for Raman characteristic peak P_I^1, P_I^3, P_I^6, P_I^{11}, P_I^{12}, P_I^{14}, P_I^{17}.

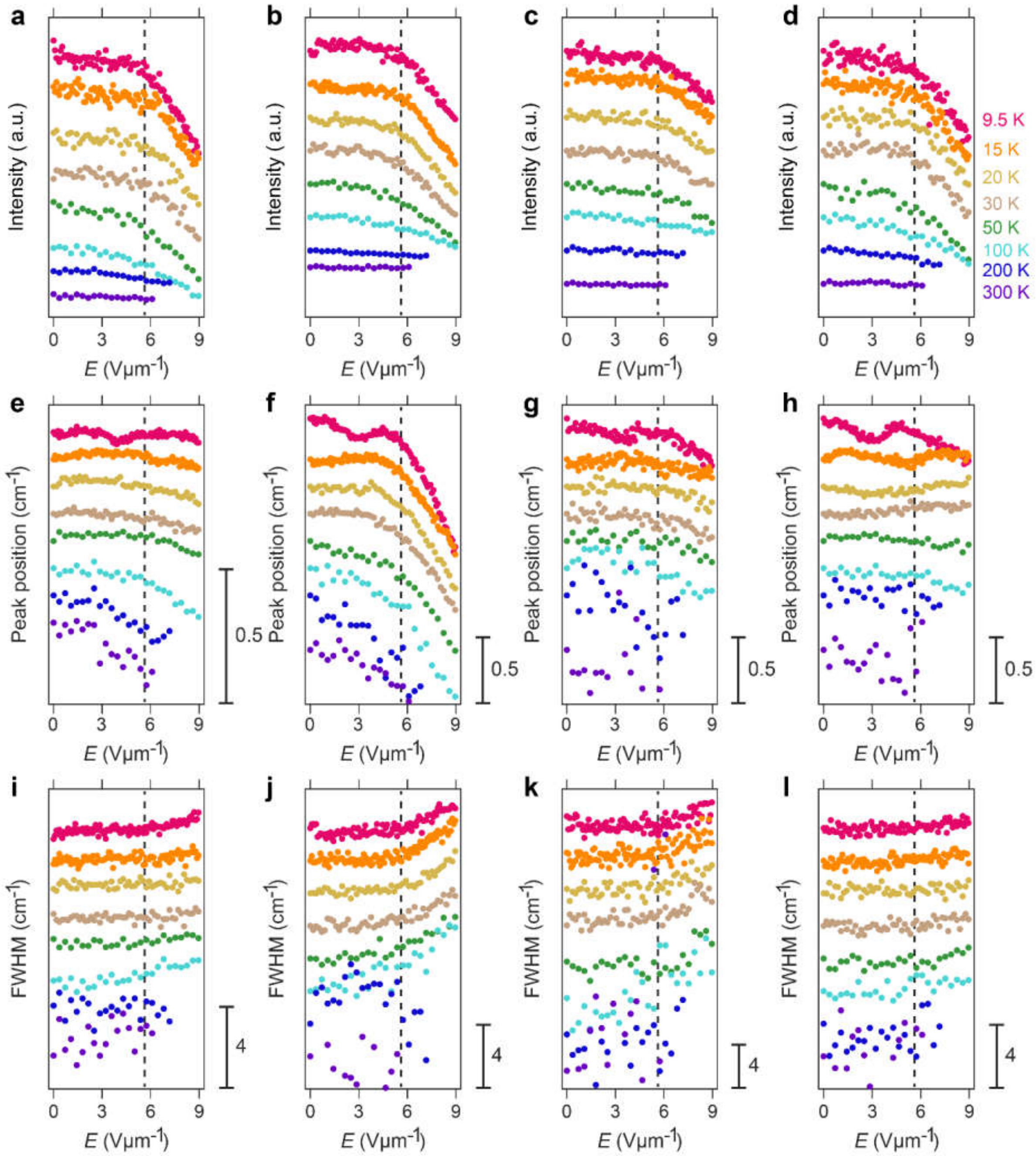

Supplementary Figure 47. Electric-field dependent Raman characteristic peak response of phase I in Device #R3 under XY configuration. a-d Electric-field dependent intensity response under XY configuration for Raman characteristic peak P_I^6, P_I^{11}, P_I^8, P_I^{12}. **e-h** Electric-field dependent peak position response under XY configuration for Raman characteristic peak $\mathrm{P_I^6}$, $\mathrm{P_I^{11}}$, $\mathrm{P_I^8}$, $\mathrm{P_I^{12}}$. **a-d** Electric-field dependent FWHM response under XX configuration for Raman characteristic peak $\mathrm{P_I^6}$, $\mathrm{P_I^{11}}$, $\mathrm{P_I^8}$, $\mathrm{P_I^{12}}$.

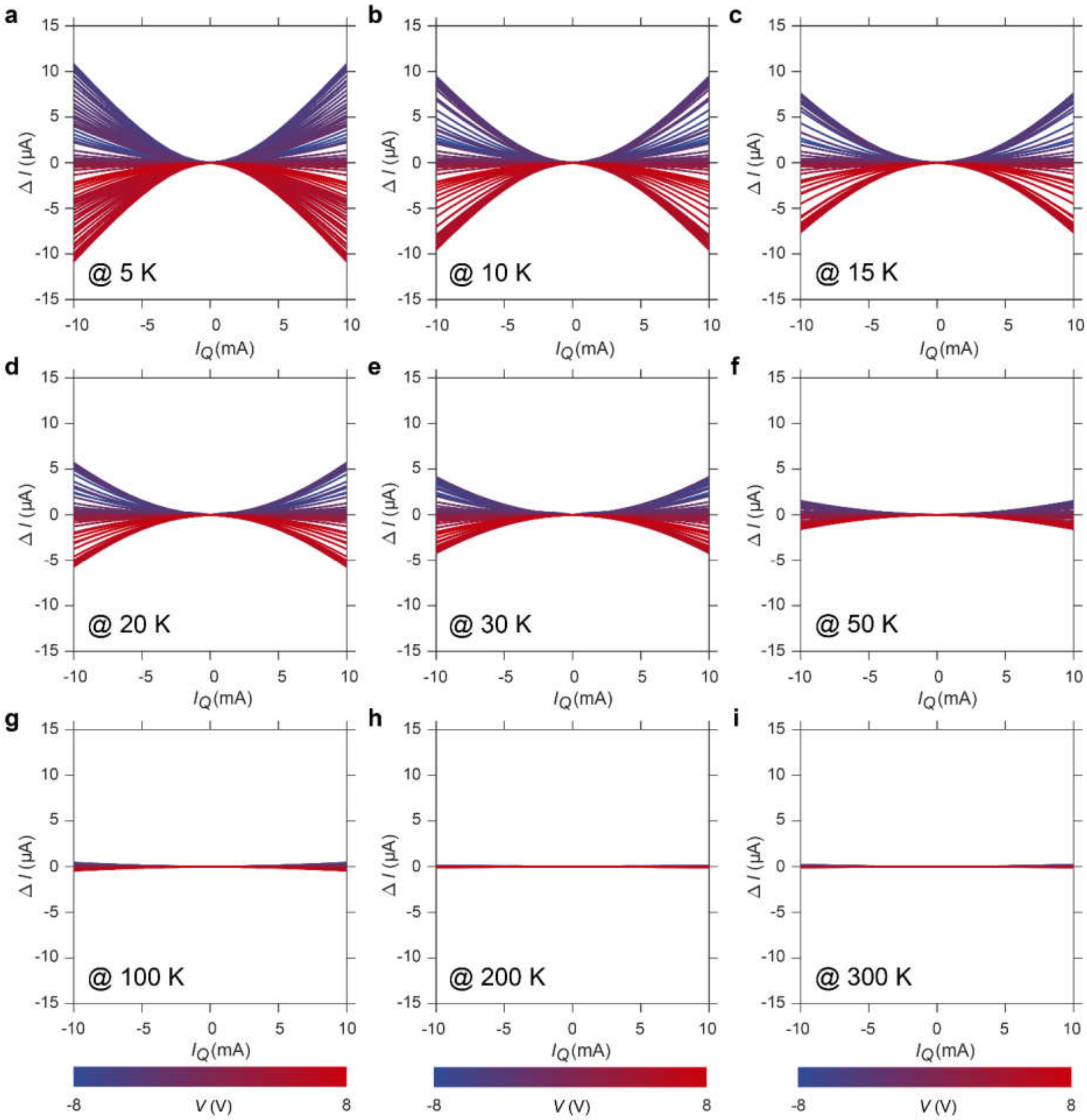

Supplementary Figure 48. Original data of field-TIC (FTIC) under different electric voltage and temperatures in Device #3. a-i Original data of FTIC under different electric voltage in Device #3 at temperature range from 5 K to 300 K.

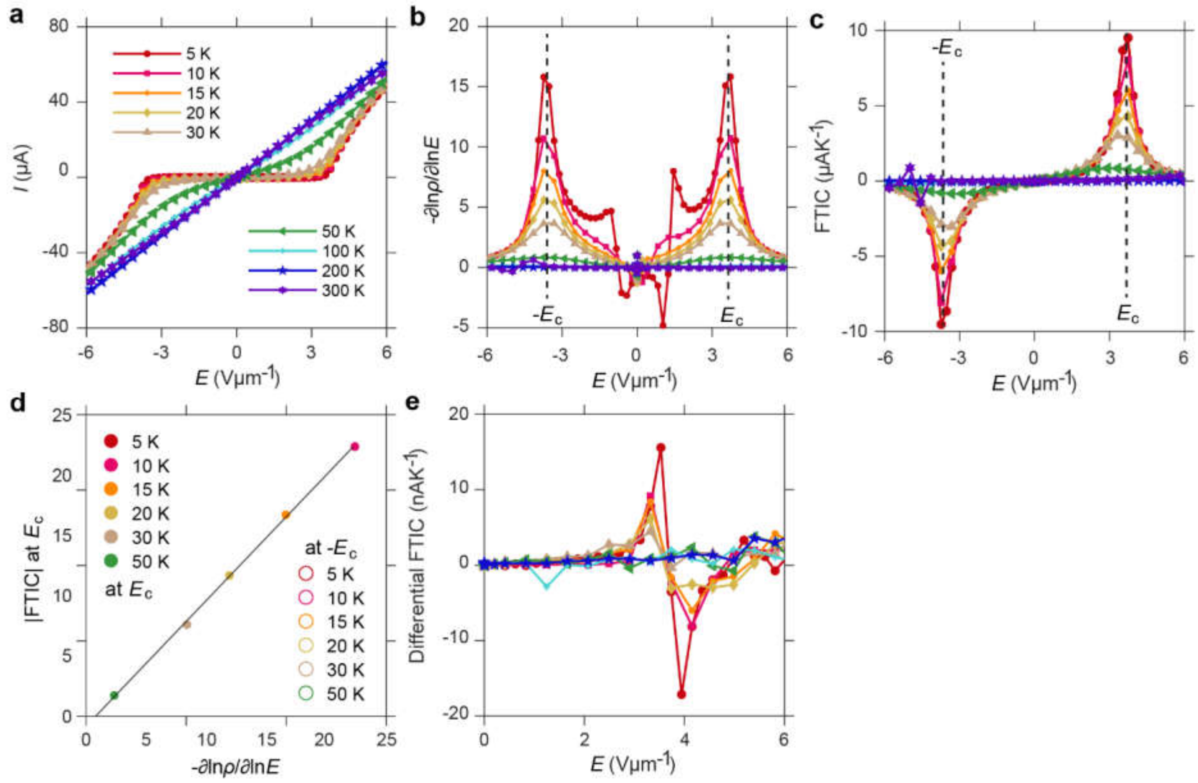

Supplementary Figure 49 FTIC in Device #16. a-c Electric-field-current characteristic curves (**a**), Electric-field dependent carrier activation energy (**b**) and FTIC (**c**) of phase I under different temperatures in Device #16. **d** Linear relationship between the FTIC and the electric-field dependent carrier activation energy at the critical electric-field under different temperatures. **e** Differential FTIC of phase I under different temperatures in Device #16.

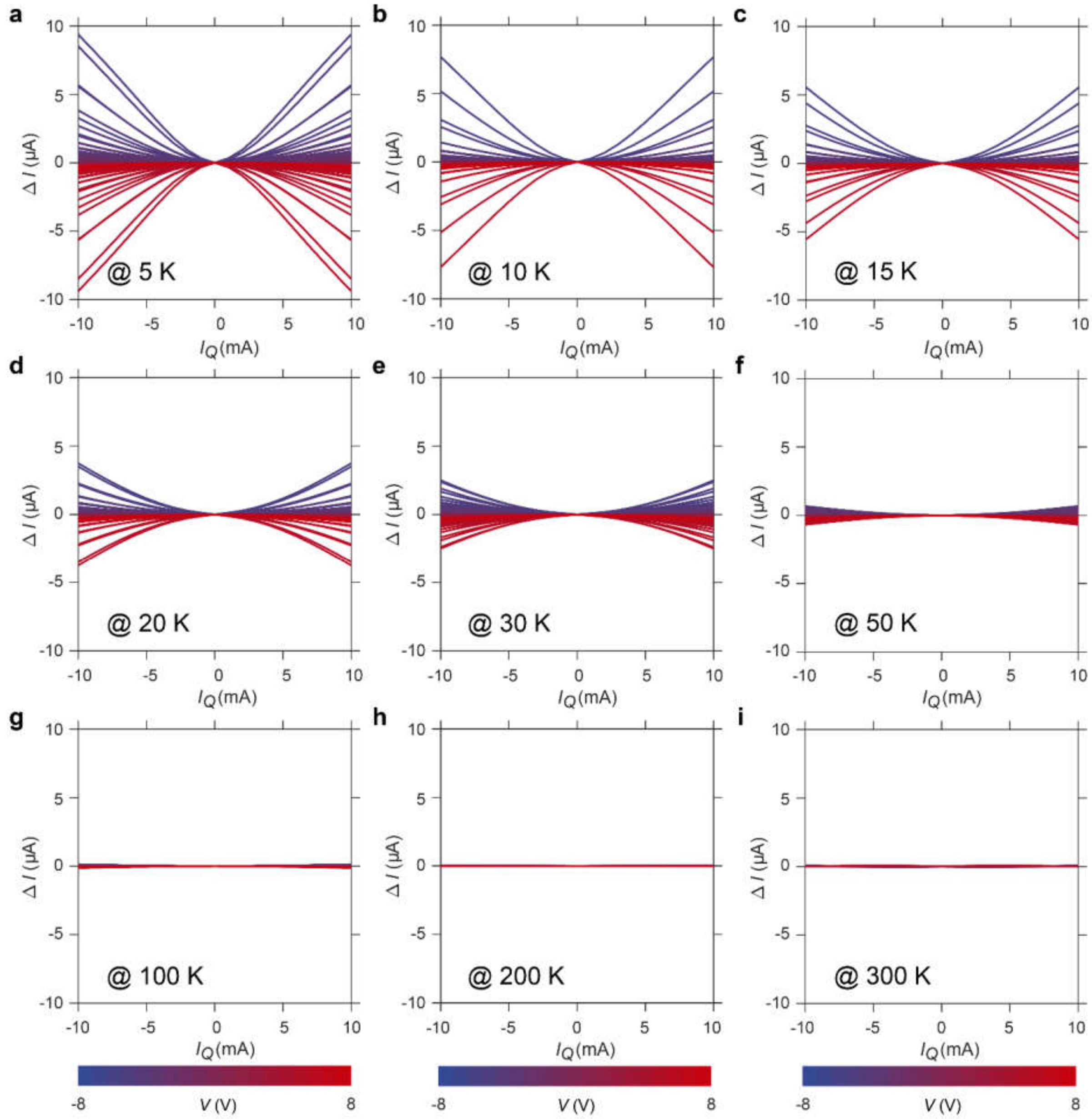

Supplementary Figure 50. Original data of FTIC under different electric voltage and temperatures in Device #16. a-i Original data of FTIC under different electric voltage in Device #16 at temperature range from 5 K to 300 K.

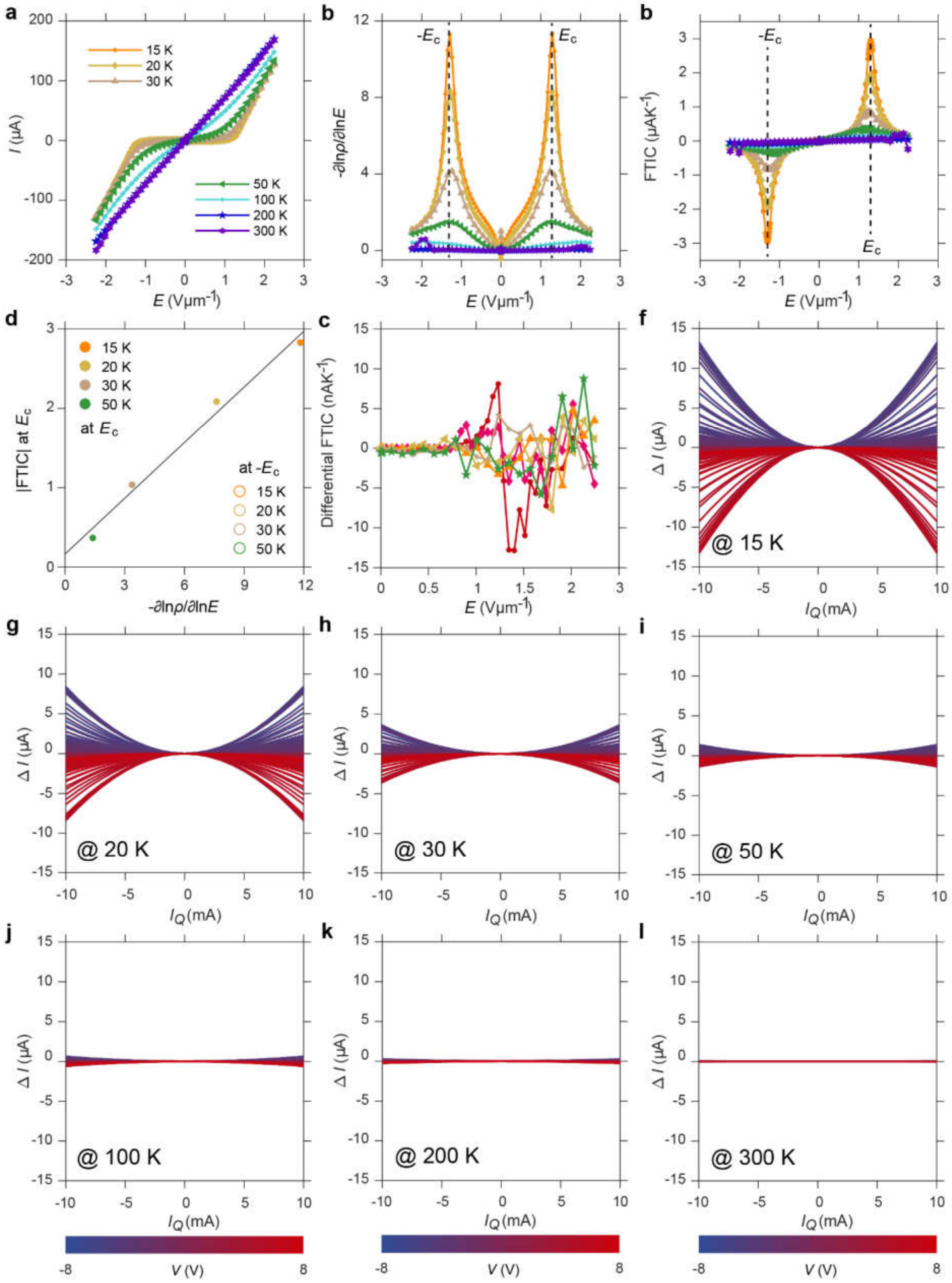
a
I (μA)
E (Vμm-1)
15 K
20 K
30 K
50 K
100 K
200 K
300 K
b
-∂lnρ/∂lnE
-Ec
Ec
E (Vμm-1)
b
FTIC (μAK-1)
-Ec
Ec
E (Vμm-1)
d
|FTIC| at Ec
-∂lnρ/∂lnE
15 K
20 K
30 K
50 K
at Ec
at -Ec
15 K
20 K
30 K
50 K
c
Differential FTIC (nAK-1)
E (Vμm-1)
f
Δ I (μA)
IQ (mA)
@ 15 K
g
@ 20 K
h
@ 30 K
i
@ 50 K
j
@ 100 K
k
@ 200 K
l
@ 300 K
V (V)
-8
8

Supplementary Figure 51 FTIC in Device #14. a-c Electric-field-current characteristic curves (**a**), Electric-field dependent carrier activation energy (**b**) and FTIC (**c**) of phase I under different temperatures in Device #14. **d** Linear relationship between the FTIC and the electric-field dependent carrier activation energy at the critical electric-field under different temperatures. **e** Differential FTIC of phase I under different temperatures in Device #14. **f-l** Original data of FTIC under different electric voltage in Device #16 at temperature range from 15 K to 300 K.

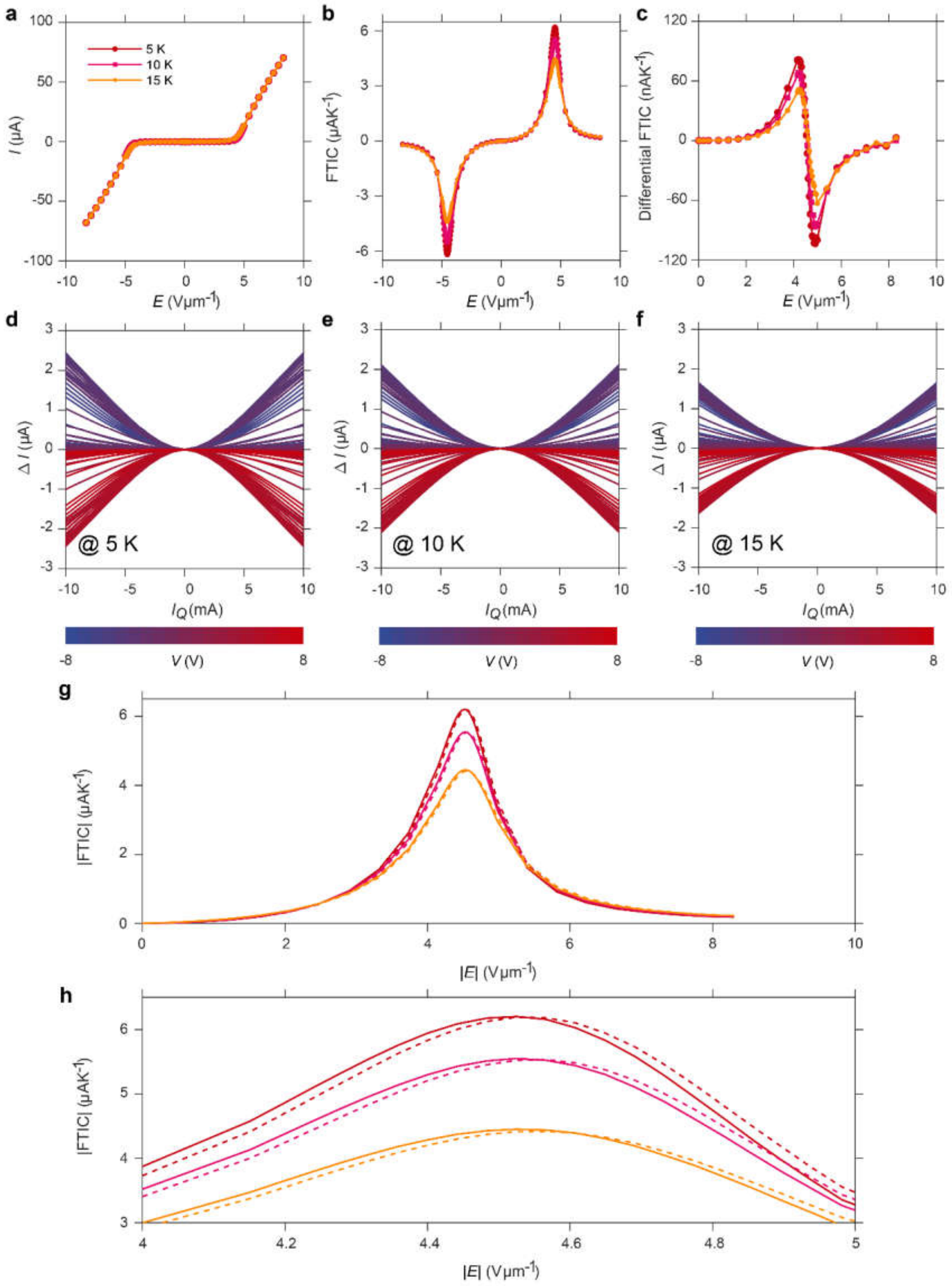

Supplementary Figure 52 FTIC in Device #15. a-b Electric-field-current characteristic curves (**a**) and FTIC (**b**) of phase I under different temperatures in Device #15. **c** Differential FTIC of phase I under different temperatures in Device #15. **d-f** Original data of FTIC under different electric voltage in Device #16 at temperature range from 5 K to 15 K. **g**,**h** A zoom in image of the FTIC shoulder in the Supplementary Figure 50b. The solid line represents the FTIC in the positive electric-field, and the dashed line represents the absolute value of the FTIC in the negative electric-field.

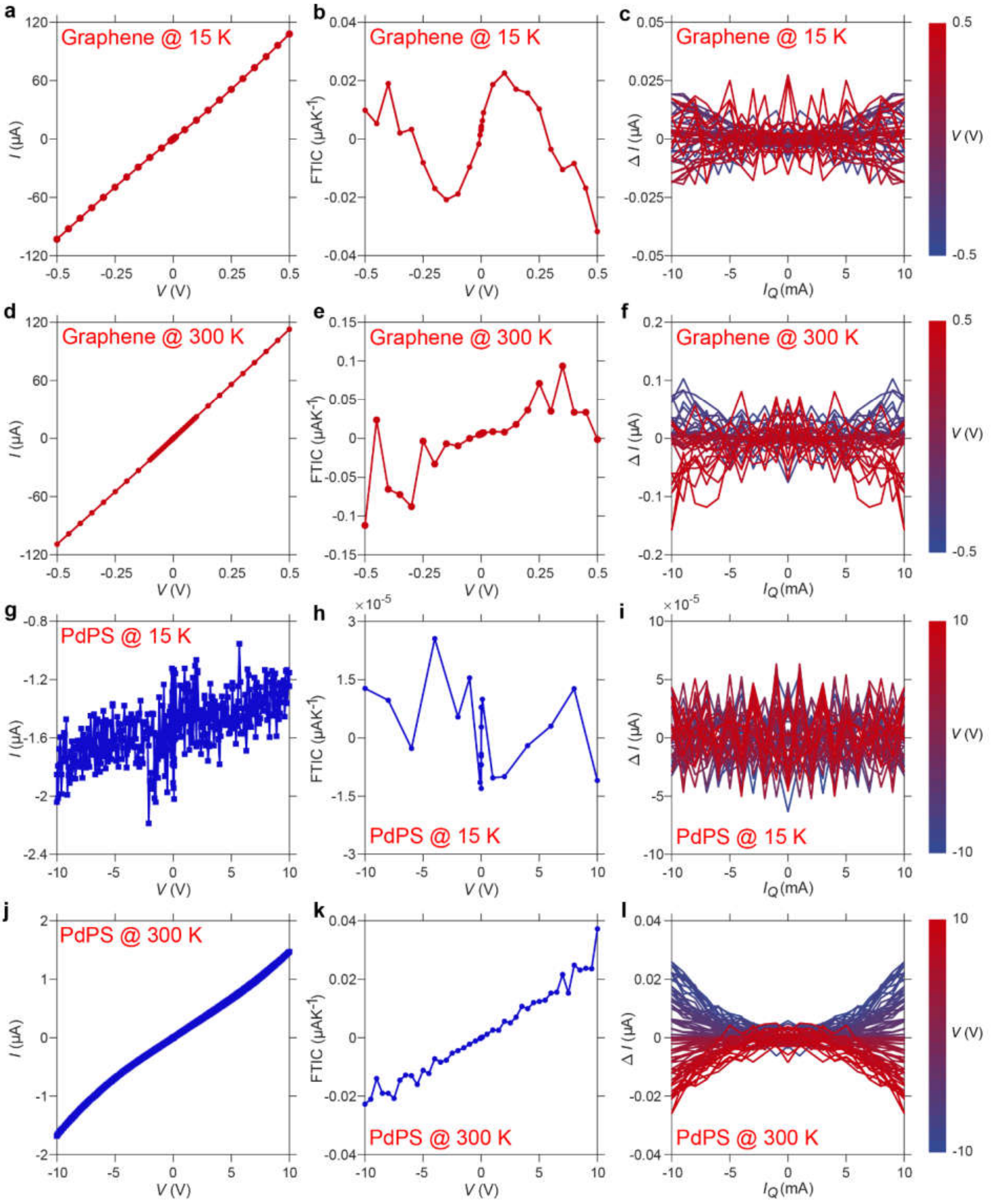

Supplementary Figure 53 FTIC in Device #20 and #21. a-c Electric voltage-current characteristic curves (**a**), FTIC (**b**) and the original FTIC of semimetal Graphene in Device #20 at 15 K. **d-f** Electric voltage-current characteristic curves (**d**), FTIC (**e**) and the original field thermal induced current of semimetal

Graphene in Device #20 at 300 K. **g-i** Electric voltage-current characteristic curves (**g**), FTIC (**j**) and the original FTIC of semiconductor PdPS in Device #21 at 15 K. **j-l** Electric voltage-current characteristic curves (**j**), FTIC (**k**) and the originalFTIC of semiconductor PdPS in Device #21 at 300 K.

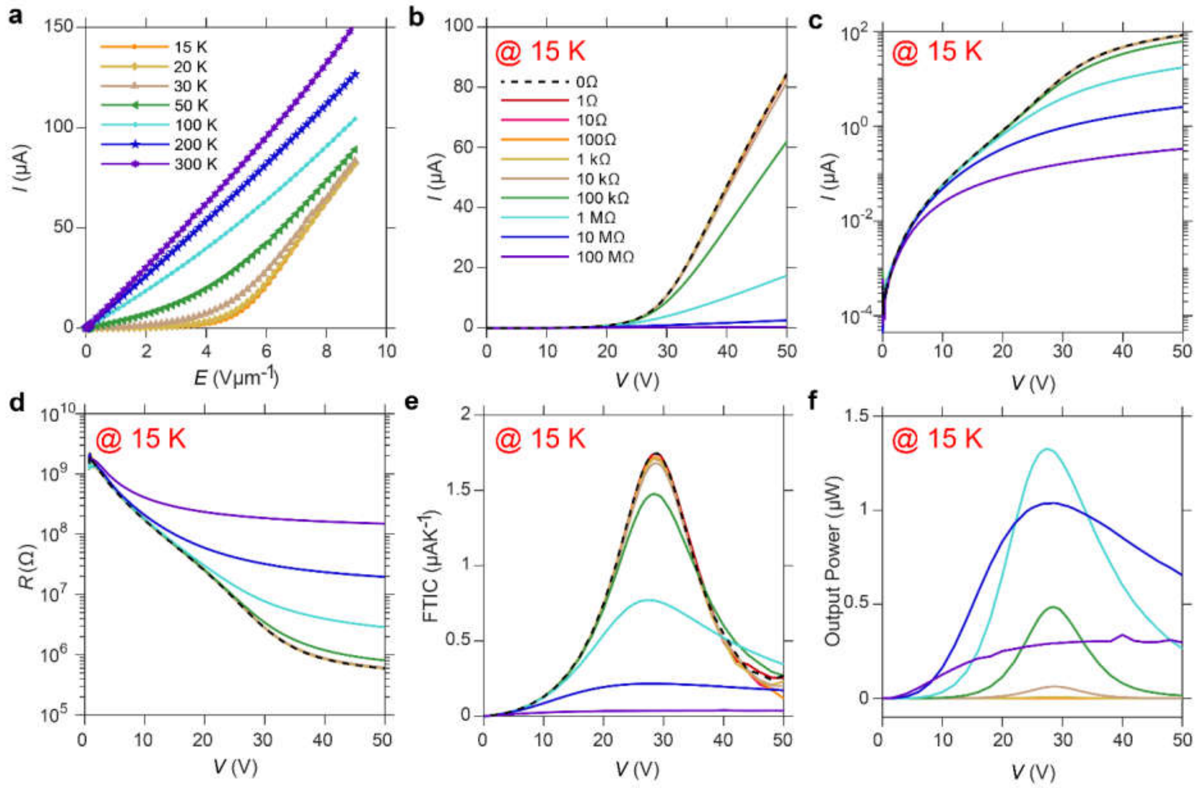

Supplementary Figure 54. Output performance of excitonic power supply demoed in Device #19. a Electric-field-current characteristic curves of phase I under different temperatures in Device #19. **b,c** Electric voltage-current characteristic curve with different power supplies under normal (**b**) and logarithmic axes (**c**). **d-f** Internal resistance (**d**), FTIC (**e**) and output power (**f**) under different voltages and power supplies.

Supplementary Tables

	XX configuration @ 8.3 K (cm^{-1})	XY configuration @ 8.3 K (cm^{-1})	XX configuration @ 300 K (cm^{-1})	XY configuration @ 300 K (cm^{-1})
P_{I}^{1}	39.65	38.75	39.12	37.86
P_{I}^{2}	44.89	42.31	48.14	too weak
P_{I}^{3}	56.62	59.23	62.84	62.42
P_{I}^{4}	74.23	72.30	72.54	71.49
P_{I}^{5}	125.29	123.49	123.89	121.20
P_{I}^{6}	127.50	126.78	125.59	123.99
P_{I}^{7}	138.43	143.15	Too weak	Too weak
P_{I}^{8}	152.26	151.02	149.99	146.00
P_{I}^{9}	Too weak	250.62	Too weak	249.46
P_{I}^{10}	262.32	261.71	259.39	257.15
P_{I}^{11}	270.76	270.54	268.16	266.87
P_{I}^{12}	292.02	291.47	291.00	289.35
P_{I}^{13}	298.75	Too weak	Too weak	Too weak
P_{I}^{14}	319.72	320.23	318.97	316.86
P_{I}^{15}	321.46	Too weak	Too weak	Too weak
P_{I}^{16}	336.74	Too weak	Too weak	Too weak
P_{I}^{17}	343.98	343.39	341.18	339.28
P_{I}^{18}	Too weak	374.47	Too weak	Too weak
P_{I}^{19}	396.36	395.77	394.35	391.88
P_{I}^{20}	417.19	415.04	413.07	412.06
P_{I}^{21}	446.15	445.76	Too weak	Too weak

Supplementary Table 1 Fitted Raman peak positions in phase I of TNS flake.

	XX configuration @ 8.3 K (cm^{-1})	XY configuration @ 8.3 K (cm^{-1})	XX configuration @ 300 K (cm^{-1})	XY configuration @ 300 K (cm^{-1})
P_{II}^{1}	17.75	16.68	16.47	15.41
P_{II}^{2}	Too weak	26.14	Too weak	Too weak
P_{II}^{3}	42.40	41.83	42.55	41.28
P_{II}^{4}	62.07	62.14	Too weak	Too weak
P_{II}^{5}	Too weak	68.01	70.58	66.69
P_{II}^{6}	74.15	75.80	77.32	76.31
P_{II}^{7}	83.58	83.39	82.24	81.51
P_{II}^{8}	98.64	99.24	99.08	99.14
P_{II}^{9}	115.51	114.76	115.48	114.36
P_{II}^{10}	120.42	120.97	118.49	117.29
P_{II}^{11}	124.74	124.83	123.32	121.65
P_{II}^{12}	145.31	144.80	143.04	143.42
P_{II}^{13}	150.77	149.51	146.58	146.35
P_{II}^{14}	214.76	212.94	Too weak	Too weak
P_{II}^{15}	248.79	246.99	238.91	243.15
P_{II}^{16}	261.83	261.17	264.83	265.23
P_{II}^{17}	271.39	270.73	Too weak	Too weak
P_{II}^{18}	293.79	294.08	291.49	292,35
P_{II}^{19}	323.33	Too weak	Too weak	Too weak
P_{II}^{20}	331.99	333.73	Too weak	334.76
P_{II}^{21}	340.95	341.74	338.30	Too weak
P_{II}^{22}	384.52	Too weak	Too weak	Too weak
P_{II}^{23}	394.49	393.59	393.64	391.62
P_{II}^{24}	416.06	Too weak	Too weak	Too weak
P_{II}^{25}	445.53	Too weak	Too weak	Too weak

Supplementary Table 2 Fitted Raman peak positions in phase II of TNS flake.

	$E_c^{\boldsymbol{b}}$ (Vμm^{-1})	$E_c^{\boldsymbol{a}}$ (Vμm^{-1})	T_{c4} (K)	T_{c3} (K)	T_{c2} (K)	T_{c1} (K)
Device #1	1.981		131.8	309.0	45.3	108.9
Device #2	3.968		84.9	332.2	43.7	108.7
Device #3	1.428					
Device #4	1.832	4.712				
Device #5	5.795	6.859				
Device #6	1.429	3.575				
Device #7	1.499	3.247				
Device #8	1.572	4.049				
Device #9	1.471	2.989				
Device #10	20.641	25.530				
Device #11	2.731					
Device #12	1.281					
Device #13	1.122					
Device #14	1.301					
Device #15	4.566					
Device #16	3.632					
Device #17				333.9	49.0	108.5
Device #18				336.0	40.7	112.9
Device #19	5.554					

Supplementary Table 3 Summary table of critical temperatures and critical electric-fields in all devices.

Supplementary Notes

Supplementary Note 1 Measurement method of TIC.

Supplementary Figure 19 shows a detailed schematic diagram of measurement method to determine the TIC. In general, the measurement consists of two key steps, measuring the thermal induced electronic current ΔI and measuring the corresponding temperature difference ΔT. The TIC is then calculated as:

$$\mathrm{TIC} = \frac{\Delta I}{\Delta T}. \tag{S1}$$

The setup for measuring of the electronic current ΔI is shown in Supplementary Figure 1a, with a representative measurement result displayed in Supplementary Figure 1b. To ensure accurate evalution under small temperature differences (~1 K), a parabolic fit is applied to the measured data, as the Joule heating is proportional to the square of the applied heating current.

The schematic for temperature difference is shown in Supplementary Figure 1c, with typical measurement results presented in Supplementary Figure 1d and e. Using the temperature dependent resistance properties of metal thermometer, we measure the in situ temperature difference corresponding to the generation of TIC. The change in resistance of a thermometer pair, induced by Joule heating, is shown in Supplementary Figure 19d. The temperature dependence of the resistance is calibrated through a controlled, slow temperature sweep, as shown in Supplementary Figure 1e. This calibriation enables accurate determination of temperature difference ΔT, which, combined with ΔI, yields the TIC.

Supplementary Note 2 Band structure of TNS under different phases obtained by first-principle calculations

In this work, we obtain the electronic band structure of TNS flake in different phases using the first-principle calculations. The results are shown in supplementary Figure 18. The band structures of the metal phase I and metal phase II phases reveal metallic characteristics, while those of the correlated phase I and correlated phase II phases exhibit semiconducting behavior.

All first-principle calculations are carried out using the Vienna Ab initio Simulation Package (VASP) with the core-electron interactions described by the projector wave-augmented method.[1,2] The Perdew-Burke-Ernzerhof parametrized generalized gradient approximation (PBE-GGA) is used for the exchange-correlation interaction.[3] The PBE+U method is adapted to descript the Hubbard interaction for Ta d orbitals,[4] the U parameter is self-consistently obtained by linear response method proposed by Cococcioni *et al*.[5] The kinetic energy cutoff of the plane wave basis is chosen to be 500 eV. The Brillouin zones are sampled by a *k*-point mesh of $8\times 8 \times 3$ and $15\times 9 \times 3$ for metal phase I, metal phase II and correlated phase I, correlated phase II, respectively. The total energy and structural relaxation convergence criteria are set to 1×10^{-6} eV and 0.01 eV/Å, respectively. In addition, DFT-D3 method with the Becke-Johnson damping function is included to account for the weak van der Wales interactions.[6,7]

Supplementary Note 3 Controlled transitions between the four reported phases in TNS flake.

Supplementary Figure 19 and 20 show the shot-by-shot evoluation of electronic conductivity measured at 15 K. A sharp decrease in conductivity is observed following each alternating current excitation pulse, whereas annealing leads to a rapid recovery of conductivity. Each subsequent excitation drives the conductivity drop to a new, lower steady-state value until another excitation pulse is applied. As the number of expciation pulse increases, the resistivity drops in a quasi-exponentially manner until reaching a local minimum value. Behond this point, neither additional excitation pulses nor increased excitation current further modify the conductivity, indicating that the change is not solely due to the electrons accumulation. Instead, the excitation currents induces a range of distinct conductivity states, consistent with the coexistence of correlated phase I and correlated phase II. These states depend on both the number and intensity of the excitation pulses. This behavior suggests an exponential growth in the volume fraction of the correlated phase I with increasing shot number or excitation intensity.

In our experiments, the amplitude of the excitation current is set to 10 mA at a frequency of 10 kHz, with each pulse applied for 5 seconds. Different amplitudes and frequencies of excitation current were tested, and it was found that when the excitation current exceeds 5 mA, it can induce consistent phase transtions. To completely transition correlated phase I to correlated phase II , an annealing treatment at 500 K for 12 hours is performed. All processes are carried out in a low-temperature cryostat under high vacuum conditions.

Supplementary Note 4 A basic fitting of the electric-field- current curve in correlated phase II of TNS flake.

The carrier current can be discribed by Boltzmann transport equation under the relaxation-time approximation as follow:

$$\begin{aligned} J^0 &= J_e^0 + J_h^0 \\ &= -\frac{e}{4\pi^3}\int \tau_e(k)v_e(k)v_e(k)[-eE]\frac{\partial f_e^0}{\partial \epsilon_e}dk \\ &\quad + \frac{e}{4\pi^3}\int \tau_h(k)v_h(k)v_h(k)[+eE]\frac{\partial f_h^0}{\partial \epsilon_h}dk \\ &= \frac{n_e e^2 \tau_e}{m_e}E + \frac{n_h e^2 \tau_h}{m_h}E. \end{aligned} \tag{S2}$$

Here, J^0, τ, v, n, m, f^0, E represent the current density, relaxation time, drift velocity, carrier concentration, effective mass, Fermi-Dirac distribution and external electric-field, respectively. The subscripts e and h represent electrons and holes respectively. We assume τ is proportional to E^{-1} under strong electric-field for EI state, and is constant after the phase transition. The electric-field induced exciton dissociation can be described by rate equation:

$$\frac{dn_e}{dt} = n_{ex}\Gamma_{dis} - n_e\Gamma_{re}. \tag{S3}$$

Here, we assume dissociation rate $\Gamma_{dis} = \Gamma_0 e^{AE}$ in which A is fitting parameter. Γ_{re} represent recombination rate and independent of E. Thus, $n_e = Be^{AE}$, where B is constant. Therefore, the current can be described as $I \sim Ce^{DE}$ under EI state and $I \sim FE$ under metal state. A fitted schematic diagram is shown in Supplementary Fig. 26.

Supplementary Note 5 Various transport phenomena in EI.

In addition to the exciton dissociation, electric-field dependent, and temperature dependent carrier activation energy discussed in detail in the main text, we present here a broader set of experimental results on transport phenomena in EI.

The first phenomenon we highlight is the highly anisotropic transport due to the anisotropy of exciton activation energy, as shown in Supplementary Figs. 28, 32, 35 to 37. The significant difference in the activation energies along the ***a***- and ***b***-axes leads to directional variation in exciton dissociation under the same electric-field. Consequently, EI may exhibit high conductivity along the ***b***-axis, while remaining insulating along the ***a***-axis, resulting in a pronounced electronic transport anisotropy. The anisotropy ratio can readily exceed 100 and is tunable via the applied electric-field, as shown in Supplementary Figure 28. This easily modifiable and large-scale anisotropy is highly promising for future anisotropic electronic applications.

The second notable transport behavior is the extraordinarily high switching ratio observed in EI. At low temperatures and low electric-fields, the system remains insulating due to the exciton condensation. In contrast, under sufficiently strong electric-fields, exciton dissociation induces a transition to a metallic state. This electric-field driven metal-insulator transition enables EIs to function effectively as electric switches, with switching ratios as high as 10^6 in most devices, and up to 10^9 in some samples (see Supplementary Figure 27). Meanwhile, the switching can be realized via a source-drain voltage, eliminating the need for a gate terminal and significantly simplifying device architecture.

A third unusual phenomenon is the the apparent length independent resistance of EI. In conventional materials, the resistivity scales linearly with the channel length due to the constant resistivity. However, in EI such as Device #12 (Supplementary Figure 29), we observe that while devices with different channel lengths have different threshold voltages, their resistance collapses onto a single curve when plotted as a function of electric-field. This implies that the resistance is governed by the electric-field rather than the physical channel length. Supplementary Figure 29c clearly shows this length independence behavior. Interestingly, although the resistance remains largely unaffected by the length, the electric-field dependent carrier activation energy increases with increasing the channellength. This behavior supports our hypothesis that TNS is an EI, as of the bose condensation of excitons becomes more robust with increasing the carrier population — effectively enhanced by longer channel lengths.

Finally, we explore the AC transport characteristics, as presented in Supplementary Figure 30 and 31. At low temperatures, the direct curren can readily disrupt the exciton condensation below 100 K. A similar but noticeably weaker effect is observed under low frequency AC measurements. As the frequency increases, a higher current amplitude is required to break the excitonic state, while the metallic conductivity becomes more pronounced. The increased critical current at higher frequencies may be attributed to the rapidly oscillating AC electric-field, which — though weaker in disrupting Coulombic interactions than DC — can more effectively perturb the condensate due to its continual direction reversal. Notably, at the low current level, the resistance curves converge due to the inability to distinguish true device resistance from the intrinsic resistance of the measurement system under near insulating conditions.

Reference

1. Kresse, G. & Furthmüller, J. Efficiency of ab-initio total energy calculations for metals and semiconductors using a plane-wave basis set. *Comput. Mater. Sci.* **6**, 15–50 (1996).
2. Kresse, G. & Furthmüller, J. Efficient iterative schemes for ab initio total-energy calculations using a plane-wave basis set. *Phys. Rev. B* **54**, 11169 (1996).
3. Blöchl, P. E. Projector Augmented-Wave Method. *Phys. Rev. B* **50**, 17953 (1994).
4. Ylvisaker, E. R., Pickett, W. E. & Koepernik, K. Anisotropy and magnetism in the LSDA+U method. *Phys. Rev. B* **79**, 035103 (2009).
5. Cococcioni, M. & de Gironcoli, S. Linear response approach to the calculation of the effective interaction parameters in the LDA+U method. *Phys. Rev. B* **71**, 035105 (2005).
6. Grimme, S., Antony, J., Ehrlich, S. & Krieg, H. A consistent and accurate ab initio parametrization of density functional dispersion correction (DFT-D) for the 94 elements H–Pu. *J. Chem. Phys.* **132**, 154104 (2010).
7. Grimme, S., Ehrlich, S. & Goerigk L. Effect of the damping function in dispersion corrected density functional theory *J. Comput. Chem.* **32**, 1456 (2011).